An analysis of recorded and simulated SH wave reverberations in the upper mantle beneath the USArray

Meichen Liu[1,1,1], Jeroen Ritsema[1,1,1], and Carlos Chaves[2,2,2]

[1]University of Michigan
[2]Universidade de São Paulo

November 30, 2022

Abstract

Long-period (T > 10 s) shear-wave reverberations between the surface and reflecting boundaries below seismic stations are useful for studying the mantle transition zone (MTZ) but finite-frequency effects may complicate the interpretation of waveform stacks. Using waveform data from the USArray and spectral-element method synthetics for 3-D seismic models, we illustrate that a common-reflection point (CRP) modeling of layering in the upper mantle must be based on 3-D reference structures and accurate calculations of reverberation traveltimes. Our CRP mapping of recorded waveforms places the 410-km and 660-km phase boundaries about 15 km deeper beneath the western US than beneath the central-eastern US if it is based on the 1-D PREM model. The apparent east-to-west deepening of the MTZ disappears in the CRP image if we account for shear-wave velocity variations in the mantle. We also find that ray theory overpredicts the traveltime delays of the reverberations if 3-D velocity variations in the mantle are prescribed by global models S40RTS, SEMUCB-WM1, and TX2015. Undulations of the 410-km and 660-km are underestimated in the analysis when their wavelengths are smaller than the Fresnel zones of the wave reverberations in the MTZ.

This is a pre-copyedited, author-produced PDF of an article accepted for publication in Geophysical Journal International following peer review. The version record "Meichen Liu, Jeroen Ritsema, Carlos A M Chaves, Influence of shear-wave velocity heterogeneity on SH wave reverberation imaging of the mantle transition zone, *Geophysical Journal International* , 2022;, ggac321" is available at https://doi.org/10.1093/gji/ggac321

Influence of shear-wave velocity heterogeneity on SH wave reverberation imaging of the mantle transition zone

Meichen Liu[1,#], Jeroen Ritsema[1], and Carlos A. M. Chaves[2]

[1] Department of Earth and Environmental Sciences, University of Michigan, 1100 North University Avenue, Ann Arbor, MI 48109, USA.

[2] Departamento de Geofísica, Instituto de Astronomia, Geofísica e Ciências Atmosféricas, Universidade de São Paulo, Rua do Matão 1226, São Paulo, São Paulo, Brasil.

In original form Jan 22nd, 2022.

Abbreviated title: SH wave reverberations in a heterogeneous mantle

Corresponding author:

Meichen Liu (meichenl@umich.edu)

PhD candidate, Department of Earth and Environmental Sciences

University of Michigan

Phone: +1 (734) 510 9687

Summary

Long-period (T > 10 s) shear-wave reflections between the surface and reflecting boundaries below seismic stations are useful for studying phase transitions in the mantle transition zone (MTZ) but shear-velocity heterogeneity and finite-frequency effects complicate the interpretation of waveform stacks. We follow up on a recent study by Shearer and Buehler (2019) (SB19) of the top-side shear-wave reflection Ssds as a probe for mapping the depths of the 410-km and 660-km discontinuities beneath the USArray. Like SB19, we observe that the recorded Ss410s-S and Ss660s-S traveltime differences are longer at stations in the western US than in the central-eastern US. The 410-km and 660-km discontinuities are about 40–50 km deeper beneath the western US than the central-eastern US if Ss410s-S and Ss660s-S traveltime differences are transformed to depth using a common-reflection point (CRP) mapping approach based on a 1-D seismic model (PREM in our case). However, the east-to-west deepening of the MTZ disappears in the CRP image if we account for 3-D shear-wave velocity variations in the mantle according to global tomography. In addition, from spectral-element method synthetics, we find that ray theory overpredicts the traveltime delays of the reverberations. Undulations of the 410-km and 660-km discontinuities are underestimated when their wavelengths are smaller than the Fresnel zones of the wave reverberations in the MTZ. Therefore, modeling of layering in the upper mantle must be based on 3-D reference structures and accurate calculations of reverberation traveltimes.

Keywords : Composition and structure of the mantle; Phase transitions; North America; Body waves; Computational seismology.

1. Introduction

Recordings of long-period (T > 10 s) shear waves are useful data to map seismic discontinuities and velocity gradients in the mantle transition zone (MTZ) (e.g., Shearer, 1990). The mineral-phase transitions near depths of 410 and 660 km produce the highest amplitude shear-wave reflections from the mantle after the ScS wave arrival (e.g., Shearer & Buehler, 2019), before the SS arrival (e.g., Flanagan & Shearer, 1998), and between multiple ScS reflections (e.g., Revenaugh & Jordan, 1991) in stacks of transverse-component seismograms. We call these boundaries the "410-km discontinuity" and "660-km discontinuity" in this paper and define the MTZ as the layer of the mantle between the 410-km and 660-km discontinuities. The depths of the 410-km and the 660-km discontinuities and the thickness of the MTZ constrain the temperature and composition of the mantle (e.g., Bina & Hellfrich, 1994; Xu et al. 2008) and heat and mass transfer between the upper and lower mantle.

Most seismological studies of hundreds to thousands of waveforms are based on 1-D seismic reference profiles and ray theory to facilitate the analysis and computations. However, long-period shear waves are sensitive to seismic inhomogeneities in the mantle beyond the geometric ray so ray-theoretical calculations of traveltimes and waveform shifts may be inaccurate (e.g., Tromp et al. 2005). Modeling inaccuracies have been discussed thoroughly for the SS wave and its precursors (e.g., Neele et al. 1997; Zhao & Chevrot, 2003; Bai et al. 2012; Guo & Zhou, 2020; Koroni & Trampert, 2016, 2021), but they exist for all long-period seismic wave reflections and conversions in the MTZ, including the multiple ScS reverberations (e.g., Haugland et al. 2020) and receiver functions (e.g., Deng & Zhou, 2015).

The receiver-side shear-wave reverberation in the upper mantle is the phase of interest in this paper. It has been introduced by Shearer & Buehler (2019), a study we abbreviate as SB19 from hereon, as a new wave type for probing the upper mantle and the MTZ. Using USArray waveforms and a common-reflection-point (CRP) imaging method, SB19 estimated the depths of the 410-km and 660-km discontinuities to be 40–50 km deeper beneath the western US than beneath the central and eastern US. This is an important study outcome as it implies that the seismic contrast in the upper mantle beneath the tectonically active western US and tectonically stable central and eastern US extends into the MTZ.

SB19 used ray theory and the 1-D iasp91 velocity model to relate traveltimes to reflector depths. They acknowledged that 3-D seismic velocity heterogeneity may have a significant effect on the amplitude, coherence,

and depths of the 410-km and the 660-km discontinuities in the CRP images. In this paper, we follow up on their recommendation to investigate how 3-D velocity structure changes the interpretation of CRP imaging results and to test the hypothesis that the 410-km and 660-km discontinuities beneath the US are unperturbed. In Section 2, we confirm that the 410-km and 660-km discontinuities are 40–50 km deeper beneath the western US than the central-eastern US if the traveltime analysis is based on a 1-D reference structure. In Section 3, we explore how strongly 3-D shear-velocity inhomogeneities, as constrained by shear-wave velocity tomography, perturb reverberation traveltimes and how ray-theoretical traveltime corrections change the CRP images. In Section 4, we use spectral-element method seismograms to evaluate the accuracy of ray theory in predicting the reverberation traveltimes and whether undulations on the 410-km and 660-km discontinuities are resolvable by long-period shear wave reflections (section 4). In section 5, we discuss our key findings.

2. Mapping the 410-km and 660-km discontinuities by 1-D common reflection point imaging

2.1 The Ssds phase

A shear-wave reverberation beneath the receiver is abbreviated here as "Ssds", following the notation of SB19. Ssds is a shear wave that follows a similar path in the mantle as the direct S wave and reflects off the free surface and off the top of a reflector at depth d before it is recorded by a seismometer on the surface (Figure 1). The arrival time of Ssds after S depends primarily on d and the shear-wave speed above the reflecting layer. For PREM (Dziewonski & Anderson, 1981), an earthquake at the surface, and an epicentral distance of 80°, Ss410s and Ss660s arrive 159.6 s and 242.2 s after S, respectively. Ssds can interfere with SS precursors but the two phases have different slownesses and are distinguishable in waveforms recorded over a wide epicentral distance range. The top-side reflection sdsS near the source has the same traveltime as Ssds at any distance for a 1-D velocity structure (Figure 1). For stations at similar azimuths, source-side reflection points are virtually identical whereas the Ssds reflection points are separated beneath the arrays of stations. Therefore, variations in the Ssds traveltime are primarily due to seismic structure in the upper mantle beneath the seismic stations. There is no source-side and receiver-side ambiguity if the analysis is limited to earthquakes deeper than the reflecting boundaries of interest (Liu & Shearer, 2021) but the data set would be significantly smaller.

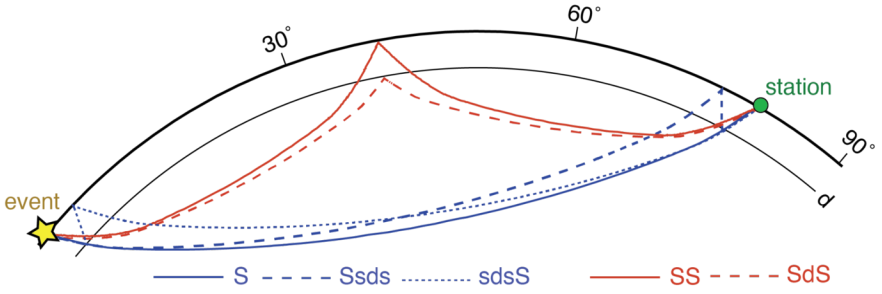

Figure 1 . Ray diagram of the phases S (solid blue line), Ssds (dashed blue line), sdsS (dotted blue line), SS (solid red line) and the SS precursor SdS (dashed red line) for an epicentral distance of 80 degrees.

2.2 USArray waveforms

To confirm SB19's imaging results, we analyze 59,517 transverse-component displacement waveforms from 337 global earthquakes (Figure 2) recorded by stations from the USArray and other regional networks in the forty-eight conterminous United States. The earthquakes are shallower than 35 km, so the direct S wave and the depth phase sS form a single pulse at long periods. The earthquakes have moment magnitudes smaller than 7.0 so rupture complexity does not affect long-period waveforms strongly. The epicentral distances are between 60° and 110° and waveforms have been filtered using a bandpass Butterworth filter with corner frequencies of 20 mHz and 80 mHz. We align the waveforms on the peak S-wave displacement and normalize

them, so the S waves have the same polarities and maximum displacements of +1. In all waveforms, the S-wave displacement is at least six times larger than the signal in the 100-second window prior to the S wave onset. The maximum and the root-mean-square displacement in the window [30 s, 220 s] after the S-wave arrival time are more than six times and three times smaller than the peak S-wave displacement, respectively. We remove earthquakes with fewer than 20 seismograms left after these quality control steps.

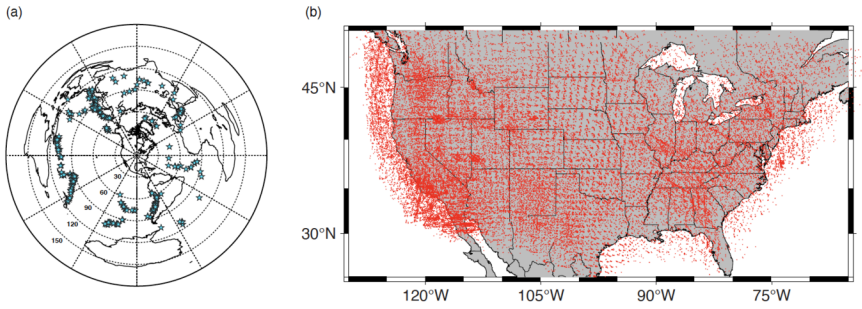

Figure 2 . (a) Epicenters of earthquakes (stars) used in this study. The dashed circles have a common center of [40°N, -95°E] and radii of 30, 60, 90, 120, and 150 degrees. (b) Red dots show reflecting points of Ss410s at the 410-km discontinuity for the 59,517 seismograms in our data set.

A record section of the sum of these waveforms brings out Ss410s and Ss660s as the strongest mantle reflections (Figure 3). The Ss410s and Ss660s have mean amplitudes of about 0.05 and are recorded without interference with ScS and SS at distances larger than 60° and 75°, respectively. The SS precursors S410S and S660S are weaker than Ss410s and Ss660s at distances smaller than 110° (e.g., Shearer, 1991). Although we cannot rule out that signals labeled 'A' and 'B' in Figure 3a are side lobes due to the applied Butterworth filter, signal 'A' may be a SS-precursor reflection at a depth of about 125 km and signal 'B' may be a Ssds reflection from the lithosphere-asthenosphere boundary (LAB), a boundary that has also been studied with P-wave and S-wave receiver functions (Rychert et al. 2007; Abt et al. 2010; Hopper & Fischer, 2018) and multiple S-wave reflection (Liu & Shearer, 2021).

Ssds reflections from the uppermost lower mantle below the 660 arrive more than 250 s after S and do not interfere with SS and the S410S precursor at distances larger than 95° in region 'C' of Figure 3a. However, it is difficult to differentiate reflections below the 660 from shallower SS precursors because S waves are attenuated by diffraction around the core and the slowness resolution is poor. The high-amplitude signal about 330 s after S waves has a slowness of roughly 1.0 sec/degree which is smaller than the slowness of any SS precursor. Its traveltime is similar to that of the phase Ss410s410s (i.e., the shear-wave reverberation with two up-and-down shear-wave segments between the surface and the 410-km discontinuity) and the phase PSs660s (i.e., the PS phase with an additional top-side reflection off the 660-km discontinuity). However, it is unlikely that these phases can be recorded with high amplitudes on transverse component records.

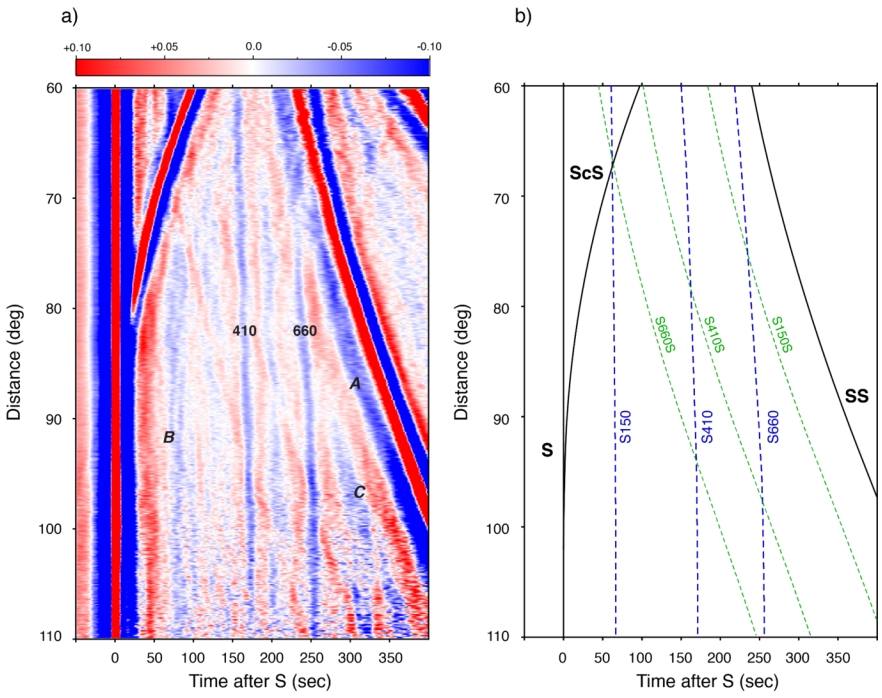

Figure 3 . (a) Record section of transverse component seismograms used in this study. Shown is the amplitude of ground displacement in red and blue for positive and negative polarities, respectively, with a color intensity proportional to the absolute value. The seismograms have been aligned to the S wave at time 0. (b) The arrival times of S, ScS, and SS (black lines), S150, S410 and S660 (blue dashed lines), and the SS-precursors S150S, S410S and S660S (green dashed lines) have been computed for PREM for a source depth of 20 km.

2.3 Common reflection point imaging

By 1-D common reflection point (CRP) mapping, we convert the Ssds-S difference times to the locations of the Ssds reflecting points in the upper 800 km of the mantle beneath the USArray. We use the TauP software (Crotwell et al. 1999) and the PREM velocity structure to calculate Ssds reflection points and traveltimes. At a depth d, 1,716 reflection points are uniformly distributed on a 1° × 1° horizontal grid between 25°N and 50°N and between -130°E and -65°E. The horizontal grids are separated by 5 km from 10 to 1,000 km, for a total of 199 depths. For a grid point X, we select waveforms for which the Ssds reflection points are within the 1° × 1° bin around X and for which the theoretical Ssds arrival time differs more than 15 s from the theoretical arrival times of sS, ScS, and sScS, and more than 50 s from the arrival time of SS to avoid wave interference. If fewer than five waveforms are available, we deem the mean displacement of Ssds to be inaccurately determined.

Since we use shallow focus earthquakes, the source-side and the receiver-side reflections have identical traveltimes. From synthetic seismograms for PREM, we have verified that they are equally strong so we attribute half of the mean Ssds amplitude to a source-side reflection. To construct the CRP images, we estimate source-side reflections of the 337 earthquakes and receiver-side reflections for the 1,716 grid points sequentially following two steps. First, we determine the mean of the Ssds displacement for each earthquake at the theoretical arrival time of Ssds. We assume that the mean displacement source-side reflection has been amplified and that receiver-side structures do not contribute coherent signals. Second, we subtract this mean value from the Ssds displacement of each waveform, assuming that the residual displacement to be due to coherent reflections beneath the USArray. We exclude events with fewer than 20 seismograms. After mapping the Ssds signals onto the grid ray theoretically, we average the receiver-side reflection amplitudes with 1°x1°

bins, which are narrower than the Fresnel zones of 10-s period Ssds reflections in the mantle transition zone, as shown by SB19. We have also implemented the approach by SB19, who estimates the source-side and receiver-side contributions to Ssds in one step using a sparse-matrix inversion solver. This approach yields smaller amplitudes of the Ssds reflections but the overall character of the CRP image, including the depths of the 410-km and 660-km discontinuities, are similar (Supplementary Figure S1).

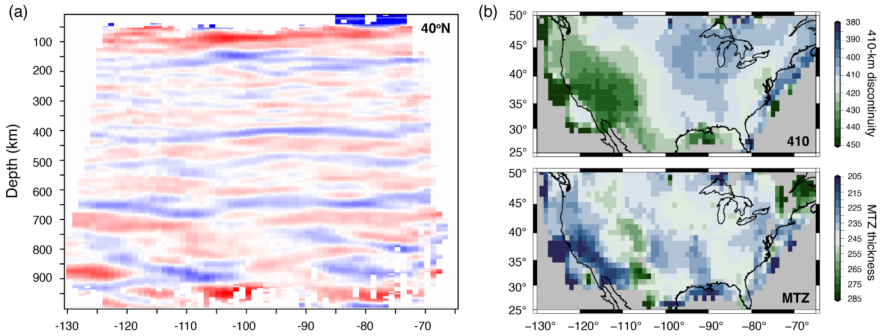

Figure 4. (a) Vertical section of the CRP image along 40°N. Blue and red colors indicate reflectors with positive and negative impedance contrasts, respectively. The color intensity is highest when the impedance contrast is strongest. All record section profiles use this color scale. (b) Depth of the 410-km discontinuity (top) and the thickness of the mantle transition zone (bottom).

Figure 4a shows a vertical section of the CRP image along the 40°N parallel. As expected from Figure 3, the 410-km and 660-km discontinuities are the clearest reflectors. Variations of the Ss410s-S and Ss660s-S difference times project as spatial variations in the depth of 410-km and 660-km discontinuities. The 410-km and 660-km discontinuities are deeper and more complex beneath the western US (west of -100°E) than beneath the central and eastern US. This is also apparent in other sections through the CRP images shown in Supplementary Figure S4. The 410-km discontinuity is strongest between longitudes -100°E and -75°E. The 520-km discontinuity may be responsible for a relatively weak Ssds reflection between the 410-km and 660-km discontinuities. The CRP images near the 410-km and 660-km discontinuities west of -100°E are complex, which was also noted by SB19. Strong reflectors corresponding to the Ssds signals in region B of the record section of Figure 3 are mapped at about 100 km and 150 km depth, but their depths and strengths vary. The incoherent structures at depths larger than 800 km are most likely imaging artifacts because these structures correspond to the amplified signals in region C of Figure 3, where S are diffracting waves and the slowness resolution is relatively poor.

Figure 4b shows maps of the depth of the 410-km discontinuity and the thickness of the MTZ. These are estimated from the absolute minimum values of the mean displacements in the CRP image in the depth ranges of 350–470 km (for the 410-km discontinuity) and 620–730 km (for the 660-km discontinuity) by cubic spline interpolation. We do not estimate the depth of the 410-km and 660-km discontinuities where a secondary absolute minimum is stronger than 40% of the absolute minimum in these depth ranges. The depth of the 410-km discontinuity varies by 40–50 km. The 410-km discontinuity is deepest beneath the southern Basin and Range and the Colorado Plateau and shallowest beneath the central plains and the Atlantic coast. The thickness of the MTZ varies less than 10 km because the 410-km and 660-km discontinuities depth variations are similar. The MTZ is thinnest beneath California and thickest beneath the Southern Rocky Mountains and the Colorado plateau. The MTZ thickness is anomalous in small regions near the margins of our model domain. This includes the extremely thin (210 km) MTZ beneath the west coast of central California which was also resolved by SB19. However, the CRP images have low resolution here because the data coverage is poor.

SB19 resolved similar maps as Figure 4b, indicating that our and SB19's data sets contain consistent variations of the Ss410s-S and Ss660s-S difference times and that estimates of the depths of the 410-km and

660-km discontinuity do not strongly depend on the applied mapping method.

The S410S and S660S precursors interfere with the reverberations (Figure 3). To test their influence, we compare CRP images with and without seismograms for which the reflecting time falls within 50 s of either of the precursors (Supplementary Figure S6). The maps of the depth of the 410-km discontinuity and the MTZ thickness are similar so interference with precursors has a minor effect on the imaging results. The large difference near the Pacific coast is due to lack of data coverage.

3. Influence of 3-D seismic heterogeneity on the CRP images

The map of the depth of the 410-km discontinuity shown in Figure 4b is reminiscent of the estimated shear-wave velocity variations in the upper mantle beneath the US from the modeling of regional S-waves (e.g., Grand & Helmberger, 1984), surface-waves (e.g., Van der Lee & Nolet, 1997), and, more recently, ambient noise (e.g., Bensen et al. 2008), P-wave polarization (Park et al. 2019) and surface-wave amplification (Eddy & Ekström, 2014; Bowden & Tsai, 2017). This indicates strongly that shear-velocity variations in the mantle affect Ss410s-S and Ss660s-S difference times and that a mapping method based on a 1-D velocity structure would overestimate undulations of the 410-km and 660-km discontinuities.

3.1 S-wave traveltime variations

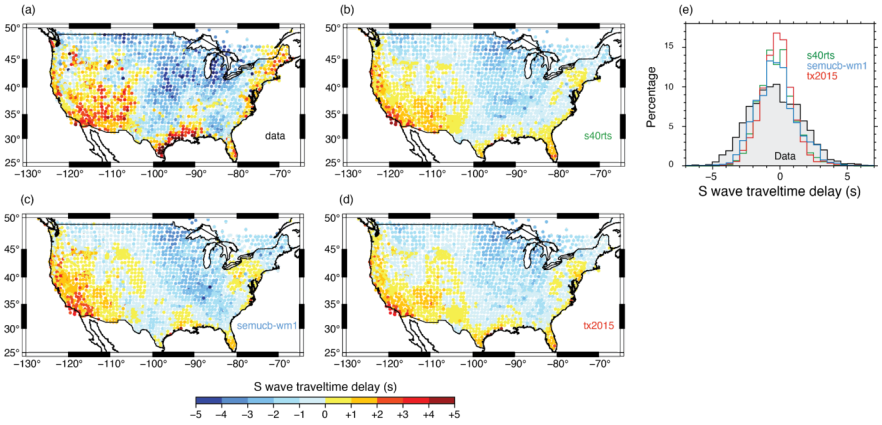

Figure 5 . The recorded (a) and predicted (b, c, d) traveltime delays of S waves by tomographic mantle models S40RTS (in b), SEMUCB-WM1 (in c), and TX2015 (in d) with crustal model CRUST1.0. Each circle indicates the location of a seismic station. Its color indicates the mean of the S-wave traveltime delays with respect to the PREM model for at least five S waves. (e) Histograms of the S wave traveltime delay in the data (gray fill) and predictions by S40RTS (green line), SEMUCB-WM1 (blue line), and TX2015 (red line) for the stations in panels a–d.

Figure 5a shows how shear-wave velocity variations in the crust using CRUST1.0 (Laske et al. 2013) and in the upper mantle affect the traveltimes of S waves. Plotted are the average S-wave delay with respect to the PREM velocity model of at least five S-waves recorded at seismic stations from the USArray. The delay times have been corrected for 'source terms', representing the effects of a potential mislocation of the earthquake location and origin time on the absolute S wave traveltime. S waves recorded by USArray stations in the western US (the tectonically active region) arrive on average 5–6 seconds later than at stations in the central and eastern US (the stable platform). The global-scale mantle models S40RTS (Ritsema et al. 2011), SEMUCB-WM1 (French & Romanowicz, 2014), and TX2015 (Lu & Grand, 2016) predict a similar traveltime pattern (Figures 5b–d) but the range is slightly smaller than in the data (Figures 5e). Our calculations indicate that the crustal structure from CRUST1.0 enhances the east-west contrast only slightly, so wave speed variations in the mantle are primarily responsible for the S-wave traveltime differences.

The imperfect match between the recorded and the predicted S wave traveltime is expected because tomographic models do not perfectly explain the recorded traveltime variation of any shear wave (e.g., Ritsema et al. 2004). Nevertheless, it is obvious that shear-velocity heterogeneity affects teleseismic S wave traveltimes across the USArray. Since Ssds has two additional propagation legs through the upper mantle, the Ss410s-S and Ss660s-S difference times are likely to be double the variation shown in Figure 5a due to shear velocity heterogeneity only. If shear-wave speed variations in the upper mantle beneath North America are ignored in the modeling, a variation of the Ss410s-S and Ss660s-S difference times of more than 10 s would imply that the depths of the 410-km and 660-km discontinuities vary by about 18 and 20 km or more. This is of the same magnitude as resolved in Figure 4.

3.2 Ray-theoretical corrections

Since the tomographically predicted S-wave traveltime variation of 5–6 seconds across the USArray is a significant fraction of the recorded traveltime variation, we suspect that shear-velocity variations in the upper mantle influence the CRP imaging and our estimate of the depth of the 410-km discontinuity. To quantify this, we determine the CRP image for "corrected" Ssds-S difference times. From the measured Ssds-S difference time, we subtract the predicted difference time anomaly (positive or negative) by shifting the waveform around the theoretical Ssds arrival time. We predict the Ssds-S difference time by ray tracing through tomographic model S40RTS for the mantle and CRUST1.0 for the crust. The Ssds-S difference time predictions are similar for SEMUCB-WM1 and TX2015, as expected from Figure 5.

Figure 6a shows the CRP image along the 40°N parallel after traveltime corrections. The character of the corrected (Figure 6) and uncorrected (Figure 4) CRP images are the same, but the 410-km and 660-km discontinuities are flatter boundaries across the USArray. This is especially clear for the region between -100°E and -80°E where the 410-km and 660-km discontinuities are relatively simple. Figure 6b emphasizes that the depth variation of the 410-km discontinuity is much smaller when the CRP image is based on tomographically corrected Ssds-S difference times. The 410-km discontinuity is not deeper in the west than in the east. The thickness of the MTZ in the corrected and uncorrected images are similar because shear-velocity variations are relatively weak in the MTZ compared to the uppermost mantle. The histograms shown in Figures 6c illustrate that the depth variation of the 410-km discontinuity is about a factor of two smaller when traveltime corrections have been applied to the data and that the corrections do not change the range in MTZ thickness values. The traveltime corrections change the mean depth of the 410-km and 660-km discontinuities by about 10 km, which is similar to the change obtained by Shearer & Buehler (2019) using ray-theoretical corrections computed for a regional 3-D velocity model.

The ray-theoretically corrected images may not reflect the actual depth variations of the 410-km discontinuity. Since S40RTS and any other tomographic model does not perfectly explain the recorded S-wave traveltime variation (see Figure 3), it is unlikely that the traveltime corrections have completely removed the effects of the shear-velocity structure on the CRP image. Further, we show in the next section that ray-theoretical predictions of long-period Ssds-S traveltimes are inaccurate and that corrections can project as spurious signals in the CRP images.

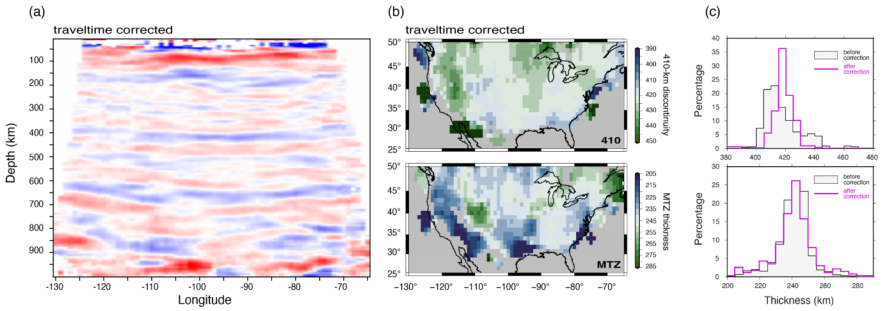

Figure 6 . Depth of the 410-km discontinuity (in a) and the thickness of the transition zone (in b) estimated after ray-theoretical traveltime corrections have been applied. The color scale in a is the same as Figure 4a. Panels c and d show histograms of the resolved depth of the 410-km discontinuity and the thickness of the MTZ beneath the USArray with (black line) and without (purple line) traveltime corrections. Compare with Figure 4b.

4. Resolution tests using spectral-element-method waveforms

We analyze synthetic waveforms to test the robustness of our CRP imaging approach, the resolution of 410-km and 660-km discontinuities undulations from long-period Ssds waveform data, and the accuracy of ray-theoretical corrections. The waveforms are computed using the SPECFEM3D-Globe software (e.g., Komatitsch & Tromp, 2002; Komatitsch et al. 2016) modified by us to allow for undulations of the 410-km and 660-km discontinuities. The eight test structures are PREM, S40RTS (Figure 7a), SEMUCB-WM1, TX2015, and structures T2, T5, T8 (Figure 7b), and T5-410-S40. The simulations account for Earth's ellipticity and anelasticity using the Q structure of PREM. In each structure, the density and velocities in the uppermost mantle extend to the surface. We remove the crust from seismic models to suppress reverberations in the crust that complicate the waveforms following the S wave (Supplementary Figure S5).

The one-dimensional PREM structure with discontinuities at 220 km, 400 km, 670 km depth serves as a baseline model for determining artifacts in the CRP images unrelated to 3-D structure in the upper mantle. In our calculations, S40RTS, SEMUCB-WM1, and TX2015 represent models of the 3-D shear velocity structure in the mantle. We do not include the crustal structure, adopt PREM as the reference mantle structure for each of the three models, and assume the Voigt average shear-velocity variations in the anisotropic SEMUCB-WM1 model. The 220-km, 410-km and 660-km discontinuities are horizontal boundaries at the same depths as in the PREM model. Models T2, T5, and T8 have the same layered velocity structure as PREM but the 410-km and the 660-km discontinuities are sinusoidal boundaries with amplitudes of 15 km and wavelengths of 2°, 5°, and 8°, respectively. The undulations of the 410-km and 660-km discontinuities are oppositely directed so the thickness of the MTZ varies up to 30 km with respect to the average of 270 km. The model T5-410-S40 has the 3-D shear velocity structure of S40RTS and sinusoidal undulations of the 410-km discontinuity with a wavelength of 5°. The 660-km discontinuity is a horizontal boundary in T5-410-S40.

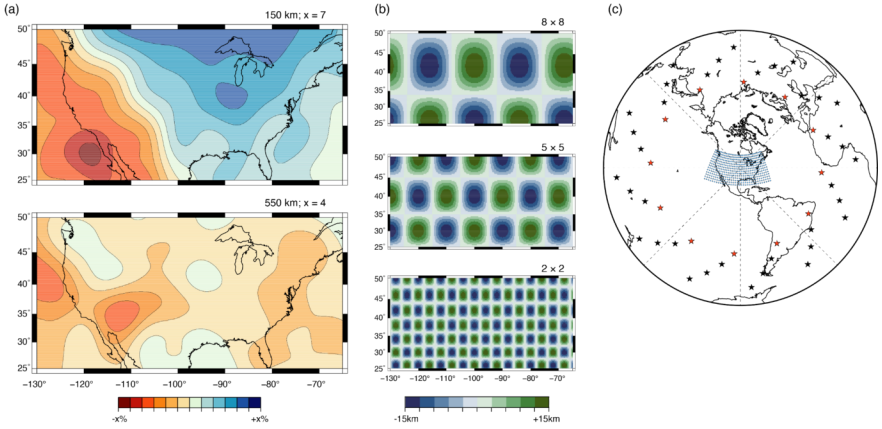

Figure 7 . (a) Maps of the shear-velocity variation at (top) 150 km and (bottom) 500 km depth according to S40RTS. The east-west contrast across the US is similar for SEMUCB-WM1 and TX2015. (b) Harmonic undulations of the 410-km and 660-km discontinuities for (from top to bottom) models T8, T5, and T2 with spatial wavelengths of 8°, 5°, and 2°. (c) Distribution of hypothetical earthquakes (stars) and stations (circles). For models PREM, S40RTS, T8 and T5 we compute waveforms for the twelve earthquakes indicated by red stars. For T2, we compute waveforms for these earthquakes and the additional 36 earthquakes indicated by black stars.

For each of the eight structures, we compute waveforms at periods longer than 10 s for 462 stations in a rectangular 2° 2° grid between longitudes 130°–65°W and latitudes 25°–50°N (Figure 7c). We calculate waveforms for 12 earthquakes uniformly distributed at a distance of 75° from [-100°E, 40°N]. We use 48 earthquakes distributed in a spiral for structure T2. All earthquakes have the same dip-slip source mechanism (source parameters for event 080596G in the Global CMT catalog) to ensure strong radiation of SH waves to teleseismic stations. The uniform data coverage is sufficient to investigate the effects of velocity heterogeneity on Ssds-S traveltimes and the resolution of undulations of the 410-km and 660-km discontinuities using long-period Ssds reflections. Because of the high computational cost, we cannot afford to reproduce the source-station combinations in the data and, therefore, we cannot estimate CRP mapping artifacts due to inhomogeneous slowness and azimuthal sampling.

4.1 Testing ray-theoretical traveltime corrections

Figure 8 shows the CRP images along the 35°N parallel in the central region of the model domain determined for the PREM and S40RTS models. Supplementary Figure S2 shows similar CRP images for SEMUCB-WM1 and TX2015. The CRP image for PREM in Figure 8a is the ideal case as the assumed velocity structure of the mantle is identical to the structure used to calculate traveltimes and ray paths. Artifacts are entirely due to the implementation of the CRP mapping procedure, the limited frequency band of the waveforms, and wave interference. PREM's velocity discontinuities at 220, 400, and 670 km depth are resolved about 10 km shallower in the mantle because the crust is not included in the waveform computations. Since the waveforms are computed for periods longer than 10 s and since shear wave speed increases with depth, reflectors at larger depths are more stretched than at shallower depths. The imaged 660-km discontinuity is therefore only about 60% stronger than the imaged 410-km discontinuity even though the impedance contrast at the 660 is a factor of two stronger than at the 410-km discontinuity. The CRP image derived from PREM waveforms is mostly free of artificial layering between 150 km and 750 km depth. The side lobes of the 660 near -65°E are artifacts near the boundaries of the station grid. Layering near 100 km depth, which is especially strong near the center of the CRP image, shows that the Ssds reverberation is not an ideal wave type for imaging the uppermost mantle. The arch-shaped structure below 750 km depth is likely the projection of shallow SS precursors misinterpreted as Ssds reflections deep in the transition zone as discussed in section 2.1.

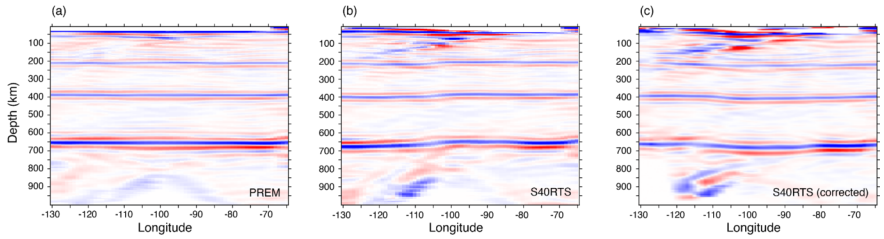

Figure 8 . CRP images along the 35°N parallel determined for (a) PREM synthetics, (b) S40RTS synthetics, and (c) S40RTS synthetics after ray-theoretical corrections have been applied. The color scale is the same as Figure 4a.

The CRP image derived from S40RTS waveforms is more complex (Figure 8b). The 410-km and 660-km discontinuities deepen from east to west because S40RTS predicts that Ssds traveltimes through the upper mantle are shorter beneath the central and eastern US than beneath the western US and we use the PREM velocity structure to convert traveltimes to reflector depths. The velocity heterogeneity in S40RTS causes misalignments of Ssds signals and therefore fluctuations in the strength of the 410-km and the 660-km discontinuities from west to east by up to a factor of two. For example, the 660 appears as a relatively weak reflecting boundary between longitudes -120°E and -110°E, near the transition between the low-velocity upper mantle of the western US and the high-velocity upper mantle beneath the central US. In addition, spurious reflectors are particularly strong between -120°E and -100°E, where horizontal gradients in the uppermost mantle are strongest. It is difficult to identify how complex wave propagation produced the complexity in

the CRP image, but the CRP image based on USArray waveforms is also most complex for the western US, and a tilted reflective structure in the upper mantle has been observed by SB19 in their data image, albeit with an eastward dip and a greater depth extent.

Figure 8c shows the CRP image based on the S40RTS synthetics after applying ray-theoretical traveltime corrections following the procedure outlined in section 4.3. The traveltime corrections do not remove, and may even amplify the CRP image artifacts for depths shallower than 100 km and deeper than 750 km. More significantly, the ray-theoretical calculations appear to overpredict the contribution of shear-velocity heterogeneity to the Ss410s-S and Ss660s-S traveltime differences. After traveltime corrections, the 410-km and 660-km discontinuities are projected shallower beneath the western US than the central US, opposite to the imaged depths of the 410-km and 660-km discontinuities prior to corrections.

The inaccuracy of ray theory in predicting the shear-wave traveltime perturbations is illustrated further in Figure 9. It shows the estimated depths of the 410-km discontinuity and the thickness of the MTZ based on the 1-D CRP method applied to synthetic waveforms computed for S40RTS. Supplementary Figure S3 shows that we obtain similar results for SEMUCB-WM1 and TX2015. The total variation in the depths of the 410-km discontinuity is about 15–20 km. As expected, the depth of the 410-km discontinuity (Figure 9a) mimics the shear-velocity variations in the upper mantle of S40RTS (Figure 7a) and the S-wave traveltime delay map shown in Figure 5. Variations in the thickness of the MTZ (Figure 9b) of about 10 km are small compared to the depth variations of the 410-km and 660-km discontinuities because shear velocity variations in the MTZ are much weaker than in the uppermost mantle.

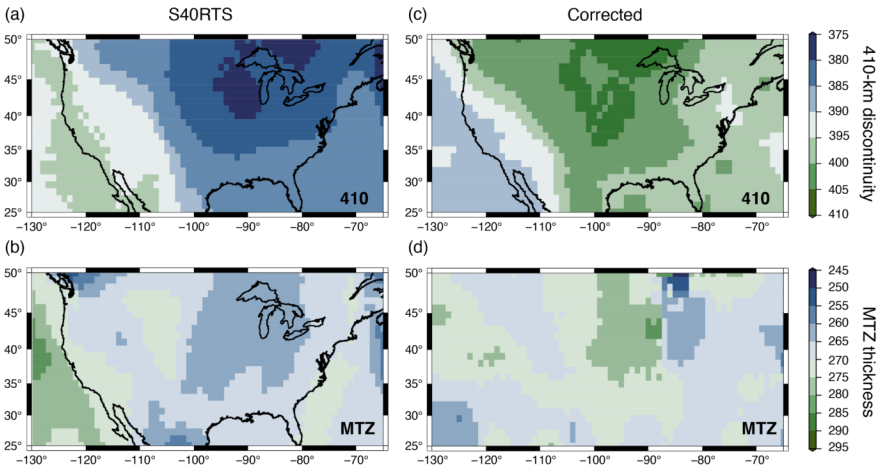

Figure 9 . Depths of the 410-km discontinuity (top row) and the thicknesses of the transition zone (bottom row). Panels (a) and (b) are estimated from spectral-element-method seismograms calculated for model S40RTS. Panels (c) and (d) show the same estimates after ray-theoretical corrections have been applied to the waveforms.

If ray-theoretical traveltime corrections are precise, we must expect that the CRP images of the ray-theoretical corrected S40RTS, SEMUCB-WM1, and TX2015 waveforms are similar to the CRP image for the PREM model because the 410-km and 660-km discontinuities are horizontal boundaries in all models. However, we find this not to be the case. While the elevation of the 410-km and 660-km discontinuities beneath the western US (by 10 and 11 km, respectively) and their depressions beneath the central-eastern US (by 11 and 12 km, respectively) have the expected trends, the corrections are larger than expected ray-theoretically. In the corrected image, the 410-km discontinuity is shallower in the western US than in the eastern US (Figure 9c) opposite to the uncorrected CRP image (Figure 9a). In the western US, the inferred and predicted depth correction differ by a factor of 1.7. The MTZ thickness has a smaller variation than the depth of the 410-km discontinuity (Figure 9c and 9d). After corrections, a larger area has a thickness within

265-275 km. The corrected Pacific coast changes from thicker to slightly thinner than the surrounding area, and the central US has the largest thickening by about 15 km.

4.2 The resolution of undulations on the 410-km and 660-km discontinuities

Figure 10 shows the depths of the 410-km and the 660-km discontinuities and the thickness of the MTZ resolved for models T2, T5, and T8. The checkerboard pattern of the undulations on the 410-km and 660-km discontinuities are resolved for T5 and T8 but the amplitude of the undulations is underestimated. The resolved thickness of the MTZ varies, on average, 12 km and 6 km less than in the original T8 and T5 models. The resolution of the undulations in T2 is poor despite using a larger set of waveforms for 48 earthquakes. From experiments, we have found that the resolution does not improve if we densify the grid of stations to a 1-degree spacing. Therefore, fluctuations of the depth of the 410-km or 660-km discontinuities with a wavelength of about 200 km are intrinsically unresolvable from long-period Ssds waveforms because the Fresnel zone of Ss410s and Ss660s in the upper mantle at the dominant frequency of about 0.05 Hz is about 500 km, much wider than the undulations of the 410-km and 660-km discontinuities in T2.

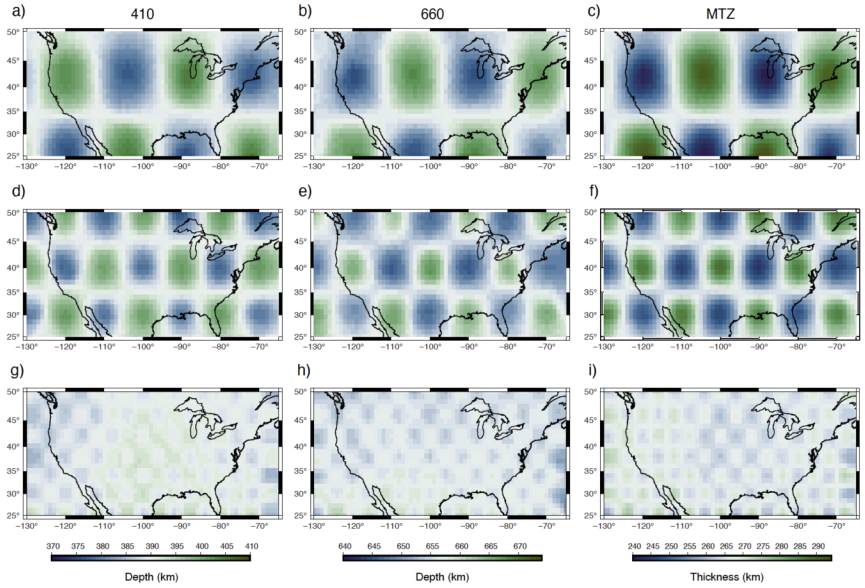

Figure 10 . Depth maps of the 410-km, 660-km discontinuities, and MTZ thickness using the CRP imaging method for 8° 8° (a, b, c) , 5° 5° (d, e, f), and 2° 2° (g, h, l) input topography models.

Figure 11 explores how undulations on the 410-km discontinuity would be resolved if they are embedded in 3-D velocity heterogeneity. We analyze waveform simulations for model T5-410-S40, described above. Figure 11 shows the resolved depth variation of the 410-km and the 660-km discontinuities and the MTZ thickness before (in a, c, and e) and after (in b, d, and f) ray-theoretical traveltime corrections have been applied to remove the effects of shear-velocity heterogeneity on the traveltimes. Figure 11a and 11b show that without traveltime corrections for 3-D heterogeneity, the resolved harmonic undulations of the 410 are overprinted by an east-to-west deepening. The ray-theoretical traveltime corrections remove the regional trend but the traveltime corrections do not accurately remove the effects of shear-velocity heterogeneity because the depth variations of the 410-km discontinuity are not perfectly resolved (compare Figures 11b and 10d). The 660-km discontinuity. a horizontal boundary in T5-410-S40, is resolved with the same east-to-west deepening without traveltime correction. After traveltime corrections, the 660-km discontinuity does not have a distinct harmonic or tectonic structure but the topography indicates that the corrections are imperfect or that the effects of the 410-km discontinuity on the traveltimes may be projected as spurious 660-km discontinuity structures. As shown also in Figure 9, the ray-theoretical corrections are too strong, but

smaller than a factor of two (Figure 9). The map of MTZ thickness, with a distorted checkerboard pattern, remains largely unchanged before and after the traveltime correction, though the checkerboard depth ranges become larger. The synthetic test of the joint effect of 3D mantle structure and undulations on the 410-km discontinuity suggests that the MTZ thickness can be determined more robustly than the absolute depths of 410-km and 660-km discontinuities using the CRP imaging approach.

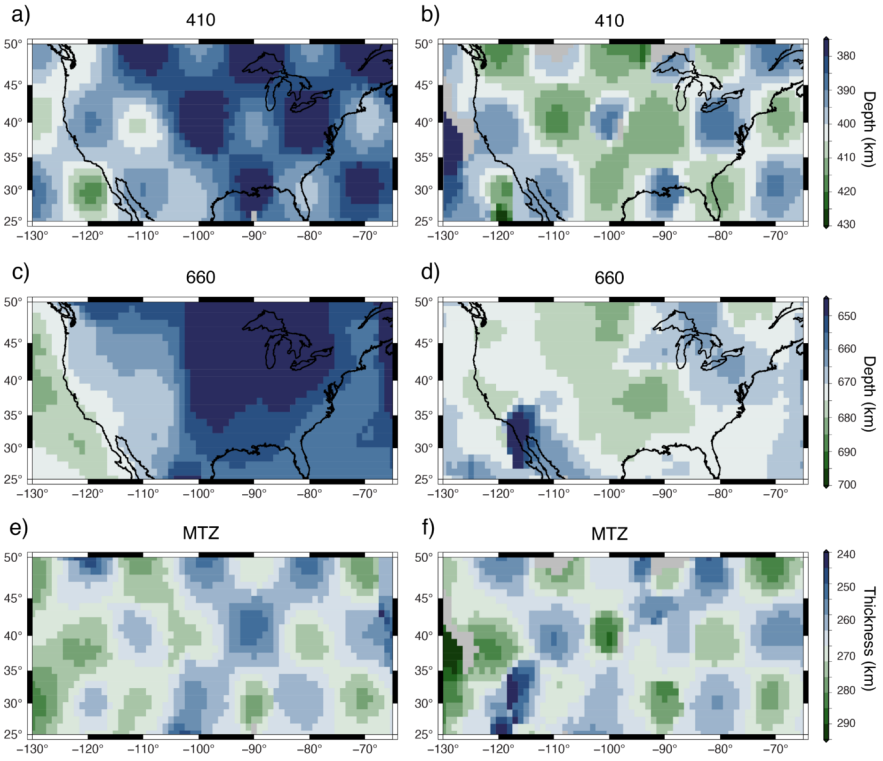

Figure 11 . Maps of the 410-km (a and b) and 660-km (c and d) discontinuities, and the thickness of the MTZ (e and f) inferred for a model with the S40RTS model velocity structure for the mantle and 5x5 harmonic undulations on the 410. In the maps along the right column (b, d, f) the effects of the velocity structure have been removed by using ray-theoretical traveltime corrections.

5. Discussion and conclusions

The receiver-side S wave reverberation, denoted as Ssds, is a useful data type to map the shear velocity structure in the upper mantle, including undulations of the 410-km and 660-km discontinuities of mineral phase transitions. Ssds complements SS precursor and P-to-S wave conversion (i.e., receiver function) imaging of the mantle because of its unique wave path geometry. In agreement with the analysis by SB19, we observe in record sections of waveform stacks that the Ss410s-S and Ss660s traveltime differences vary by up to 10 s across stations from the USArray. If the traveltime differences are attributed entirely to undulations on the 410-km and 660-km discontinuities, it implies that the 410-km and 660-km discontinuities are 40–50 km deeper beneath the western US than the central and eastern US. In turn, this would mean that the contrast between the tectonically active western US and the stable central and eastern US persists as a temperature or compositional contrast in the mantle transition zone and that there is a link between uppermost mantle and mantle transition zone dynamics.

However, the correlation between the resolved depth of the 410-km discontinuity (and the 660-km discontinuity) and tomographic maps of the shear-velocity structure in the upper mantle is high. This indicates that velocity heterogeneity in the uppermost mantle contributes significantly to the Ss410s-S and Ss660s-S

traveltimes and the spatial variations of the depth of the 410-km discontinuity inferred from CRP imaging. Ray-theoretical corrections of traveltimes for velocity heterogeneity by shifting segments of the waveforms containing Ss410s and Ss660s prior to CRP stacking reduce the variation in the depth of the 410-km discontinuity by a factor of two.

For at least two reasons we find ray-theoretical corrections imprecise. First, seismic tomography has uncertainties. Global models S40RTS, SEMUCB-WM1, and TX2015 agree on the east–west contrast but disagree on the magnitude of the traveltime perturbations (see Figure 4). Each model underestimates the S-wave traveltime delay at USArray stations (see Figure 5) which is consistent with the fact that tomographic models underestimate the magnitude of traveltime and waveform perturbations. Hence, the effect on the estimated depths of the 410-km and 660-km discontinuities depends on the chosen tomographic model. SB19 notes that the traveltime corrections may introduce incoherence in the CRP images and use that as a factor in determining the value of traveltime corrections.

Second, our experiments with spectral-element method synthetics demonstrate that ray-theoretical predictions of the Ss410s-S and Ss660s traveltime differences are inaccurate. CRP images derived from waveforms computed for a mantle with 3-D velocity heterogeneity and horizontal phase boundaries show the expected deepening of the 410-km and 660-km discontinuities below the western US and shallowing beneath the central and eastern US where the shear velocities are relatively low and high, respectively. After applying traveltime corrections for the 3-D wave speed structure, the 410 and 660 remain undulating boundaries. In fact, the 410-km and the 660-km discontinuities in the corrected CRP image are deeper beneath the central-eastern US than beneath the western US, opposite to the uncorrected CRP image. This indicates that ray theory overpredicts the Ssds-S difference time by about a factor of two. This is the case for S40RTS, SEMUCB-WM1, and TX2015 and presumably also finer-scale regional tomographic models when finite-frequency effects are stronger. The inaccuracy of ray-theoretical predictions of the traveltime perturbations of long-period waves has been studied previously. For example, Neele et al. (1997) and Zhao & Chevrot (2003) have pointed out that for the broad SS sensitivity kernels at the reflection points on the surface or the mantle discontinuities. Bai et al. (2012) and Koroni & Trampert (2016) illustrate how the finite wave effects affect CRP images built from SS precursors similarly to the study here.

Finally, we note that the resolution of the depths of the 410-km and 660-km discontinuities depends on spatial scales of the undulations. Our experiments with spectral element method synthetics indicate that the Ssds-S traveltime difference is sensitive to $5^\circ \times 5^\circ$ and $8^\circ \times 8^\circ$ sinusoidal variations of the depths of the 410-km and 660-km discontinuities albeit that the height of the undulations is underestimated. Spatial variations of the 410-km and 660-km discontinuities on a $2^\circ \times 2^\circ$ scale are not resolvable because such variations are smaller than the width of the Fresnel zone of Ssds at a period of 10 s.

Although it is beyond the scope of this work, it is better to simultaneously estimate the topography of the 410-km and 660-km discontinuities and shear velocity heterogeneity in the mantle of multiple data sets (e.g., Gu et al. 2003, Moulik and Ekström, 2014) using finite-frequency kernels that relate waveform perturbations to velocity heterogeneity and phase boundary topography (e.g., Guo & Zhou, 2020) or, preferably, using an adjoint tomography approach (Koroni & Trampert, 2021). Based on our experiments, the evidence for large-scale variations of the depth of the 410-km discontinuity beneath the USArray is weak. As is well established, estimates of the thickness of the MTZ are not affected strongly by shear velocity heterogeneity. We find the thickness of the MTZ to vary by about 10 km, which is consistent with the receiver-function study of USArray data by Gao & Liu (2014) and much smaller than global variations of the MTZ observed in SS precursors studies (e.g., Flanagan & Shearer, 1998; Chambers et al. 2005).

Acknowledgments

This research was supported by the NSF (EAR-1644829). Data from the TA network was made freely available as part of the EarthScope USArray facility, operated by Incorporated Research Institutions for Seismology (IRIS) and supported by the National Science Foundation, under Cooperative Agreements EAR-1261681. The facilities of IRIS Data Services, and specifically the IRIS Data Management Center, were used

for access to waveforms, related metadata, and/or derived products used in this study. IRIS Data Services are funded through the Seismological Facilities for the Advancement of Geoscience (SAGE) Award of the National Science Foundation under Cooperative Support Agreement EAR-1851048. The authors acknowledge the computing time provided on the AGUIA supercomputer supported by the HPC-STI (University of São Paulo). The SPECMFEM3D_Globe software was downloaded from the Computational Infrastructure for Geodynamics (*https://geodynamics.org/*). We thank the editor (Carl Tape) and two anonymous reviewers for their constructive comments.

Data availability

Information of selected 59,517 seismograms, 337 earthquakes, and source parameters of synthetic earthquakes, are deposited to the Deep Blue Data (https://doi.org/10.7302/napg-vt44).

References

Abt, D. L., Fischer, K. M., French, S. W., Ford, H. A., Yuan, H., & Romanowicz, B., 2010. North American lithospheric discontinuity structure imaged by Ps and Sp receiver functions. *Journal of Geophysical Research: Solid Earth* , *115* (B9).

Bai, L., Zhang, Y., & Ritsema, J., 2012. An analysis of SS precursors using spectral-element method seismograms. *Geophysical Journal International* , *188* (1), 293-300.

Bensen, G. D., Ritzwoller, M. H., & Shapiro, N. M., 2008. Broadband ambient noise surface wave tomography across the United States.*Journal of Geophysical Research: Solid Earth* , *113* (B5).

Bina, C. R., & Helffrich, G., 1994. Phase transition Clapeyron slopes and transition zone seismic discontinuity topography. *Journal of Geophysical Research: Solid Earth, 99* (B8), 15853-15860.

Bowden, D. C., & Tsai, V. C., 2017. Earthquake ground motion amplification for surface waves. *Geophysical Research Letters, 44* (1), 121-127.

Chambers, K., Woodhouse, J. H., & Deuss, A., 2005. Topography of the 410-km discontinuity from PP and SS precursors. *Earth and Planetary Science Letters, 235* (3-4), 610-622.

Crotwell, H. P., Owens, T. J., & Ritsema, J., 1999. The TauP Toolkit: Flexible seismic travel-time and ray-path utilities. *Seismological Research Letters* , *70* (2), 154-160.

Deng, K., & Zhou, Y., 2015. Wave diffraction and resolution of mantle transition zone discontinuities in receiver function imaging.*Geophysical Journal International, 201* (3), 2008-2025.

Dziewonski, A. M., & Anderson, D. L., 1981. Preliminary reference Earth model. *Physics of the earth and planetary interiors* ,*25* (4), 297-356.

Eddy, C. L., & Ekström, G., 2014. Local amplification of Rayleigh waves in the continental United States observed on the USArray. *Earth and Planetary Science Letters* , *402* , 50-57.

Flanagan, M. P., & Shearer, P. M., 1998. Global mapping of topography on transition zone velocity discontinuities by stacking SS precursors.*Journal of Geophysical Research: Solid Earth, 103* (B2), 2673-2692.

French, S. W., & Romanowicz, B. A., 2014. Whole-mantle radially anisotropic shear velocity structure from spectral-element waveform tomography. *Geophysical Journal International, 199* (3), 1303-1327.

Gao, S. S., & Liu, K. H., 2014. Mantle transition zone discontinuities beneath the contiguous United States. *Journal of Geophysical Research: Solid Earth* , *119* (8), 6452-6468.

Grand, S. P., & Helmberger, D. V., 1984. Upper mantle shear structure of North America. *Geophysical Journal International* ,*76* (2), 399-438.

Gu, Y.J., Dziewoński, A.M. and Ekström, G., 2003. Simultaneous inversion for mantle shear velocity and topography of transition zone discontinuities. *Geophysical Journal International, 154* (2), pp.559-583.

Guo, Z., & Zhou, Y., 2020. Finite-frequency imaging of the global 410-and 660-km discontinuities using SS precursors. *Geophysical Journal International* , *220* (3), 1978-1994.

Haugland, S. M., Ritsema, J., Sun, D., Trampert, J., & Koroni, M., 2020. Common reflection point mapping of the mantle transition zone using recorded and 3-D synthetic ScS reverberations. *Geophysical Journal International, 220* (1), 724-736.

Hopper, E., & Fischer, K. M., 2018. The changing face of the lithosphere-asthenosphere boundary: Imaging continental scale patterns in upper mantle structure across the contiguous US with Sp converted waves. *Geochemistry, Geophysics, Geosystems* , *19* (8), 2593-2614.

Komatitsch, D., & Tromp, J., 2002. Spectral-element simulations of global seismic wave propagation—I. Validation. *Geophysical Journal International* , *149* (2), 390-412.

Komatitsch, D., Xie, Z., Bozdağ, E., Sales de Andrade, E., Peter, D., Liu, Q., & Tromp, J., 2016. Anelastic sensitivity kernels with parsimonious storage for adjoint tomography and full waveform inversion. *Geophysical Journal International* , *206* (3), 1467-1478.

Koroni, M., & Trampert, J., 2016. The effect of topography of upper-mantle discontinuities on SS precursors. *Geophysical Journal International, 204* (1), 667-681.

Koroni, M. and Trampert, J., 2021. Imaging global mantle discontinuities: a test using full-waveforms and adjoint kernels. *Geophysical Journal International, 226* (3), pp.1498-1516.

Laske, G., Masters, G., Ma, Z., & Pasyanos, M., 2013. Update on CRUST1. 0—A 1-degree global model of Earth's crust. In *Geophys. res. abstr* , vol. 15, p. 2658.

Liu, T., & Shearer, P. M., 2021. Complicated Lithospheric Structure Beneath the Contiguous US Revealed by Teleseismic S-Reflections. *Journal of Geophysical Research: Solid Earth* , *126* (5), e2020JB021624.

Lu, C., & Grand, S. P., 2016. The effect of subducting slabs in global shear wave tomography. *Geophysical Journal International, 205* (2), 1074-1085.

Moulik, P. and Ekström, G., 2014. An anisotropic shear velocity model of the Earth's mantle using normal modes, body waves, surface waves and long-period waveforms. *Geophysical Journal International, 199* (3), pp.1713-1738.

Neele, F., de Regt, H., & Van Decar, J., 1997. Gross errors in upper-mantle discontinuity topography from underside reflection data. *Geophysical Journal International, 129* (1), 194-204.

Park, S., Tsai, V. C., & Ishii, M., 2019. Frequency-dependent P wave polarization and its subwavelength near-surface depth sensitivity. *Geophysical Research Letters* , *46* (24), 14377-14384.

Revenaugh, J., & Jordan, T. H., 1991. Mantle layering from ScS reverberations: 2. The transition zone. *Journal of Geophysical Research: Solid Earth, 96* (B12), 19763-19780.

Ritsema, J., Deuss, A. A., Van Heijst, H. J., & Woodhouse, J. H., 2011. S40RTS: a degree-40 shear-velocity model for the mantle from new Rayleigh wave dispersion, teleseismic traveltime and normal-mode splitting function measurements. *Geophysical Journal International* , *184* (3), 1223-1236.

Ritsema, J., Van Heijst, H.J. and Woodhouse, J.H., 2004. Global transition zone tomography. *Journal of Geophysical Research: Solid Earth, 109* (B2).

Rychert, C. A., Rondenay, S., & Fischer, K. M., 2007. P-to-S and S-to-P imaging of a sharp lithosphere-asthenosphere boundary beneath eastern North America. *Journal of Geophysical Research: Solid Earth* ,*112* (B8).

Shearer, P. M., 1990. Seismic imaging of upper-mantle structure with new evidence for a 520-km discontinuity. *Nature* , *344* (6262), 121-126.

Shearer, P.M., 1991. Constraints on upper mantle discontinuities from observations of long-period reflected and converted phases. *Journal of Geophysical Research: Solid Earth, 96* (B11), pp.18147-18182.

Shearer, P. M., & Buehler, J., 2019. Imaging upper-mantle structure under USArray using long-period reflection seismology. *Journal of Geophysical Research: Solid Earth* , *124* (9), 9638-9652.

Tromp, J., Tape, C., & Liu, Q., 2005. Seismic tomography, adjoint methods, time reversal and banana-doughnut kernels. *Geophysical Journal International, 160* (1), 195-216.

Van der Lee, S., & Nolet, G., 1997. Upper mantle S velocity structure of North America. *Journal of Geophysical Research: Solid Earth ,102* (B10), 22815-22838.

Xu, W., Lithgow-Bertelloni, C., Stixrude, L. and Ritsema, J., 2008. The effect of bulk composition and temperature on mantle seismic structure.*Earth and Planetary Science Letters, 275* (1-2), pp.70-79.

Zhao, L., & Chevrot, S., 2003. SS-wave sensitivity to upper mantle structure: Implications for the mapping of transition zone discontinuity topographies. *Geophysical research letters, 30* (11).

Influence of shear-wave velocity heterogeneity on SH wave reverberation imaging of the mantle transition zone

Meichen Liu[1,#], Jeroen Ritsema[1], and Carlos A. M. Chaves[2]

[1] Department of Earth and Environmental Sciences, University of Michigan, 1100 North University Avenue, Ann Arbor, MI 48109, USA.

[2] Departamento de Geofísica, Instituto de Astronomia, Geofísica e Ciências Atmosféricas, Universidade de São Paulo, Rua do Matão 1226, São Paulo, São Paulo, Brasil.

In original form Jan 22nd, 2022.

Abbreviated title: SH wave reverberations in a heterogeneous mantle

[#] Corresponding author:

Meichen Liu (meichenl@umich.edu)

PhD candidate, Department of Earth and Environmental Sciences

University of Michigan

Phone: +1 (734) 510 9687

Summary

Long-period (T > 10 s) shear-wave reflections between the surface and reflecting boundaries below seismic stations are useful for studying phase transitions in the mantle transition zone (MTZ) but shear-velocity heterogeneity and finite-frequency effects complicate the interpretation of waveform stacks. We follow up on a recent study by Shearer and Buehler (2019) (SB19) of the top-side shear-wave reflection Ssds as a probe for mapping the depths of the 410-km and 660-km discontinuities beneath the USArray. Like SB19, we observe that the recorded Ss410s-S and Ss660s-S traveltime differences are longer at stations in the western US than in the central-eastern US. The 410-km and 660-km discontinuities are about 40–50 km deeper beneath the western US than the central-eastern US if Ss410s-S and Ss660s-S traveltime differences are transformed to depth using a common-reflection point (CRP) mapping approach based on a 1-D seismic model (PREM in our case). However, the east-to-west deepening of the MTZ disappears in the CRP image if we account for 3-D shear-wave velocity variations in the mantle according to global tomography. In addition, from spectral-element method synthetics, we find that ray theory overpredicts the traveltime delays of the reverberations. Undulations of the 410-km and 660-km discontinuities are underestimated when their wavelengths are smaller than the Fresnel zones of the wave reverberations in the MTZ. Therefore, modeling of layering in the upper mantle must be based on 3-D reference structures and accurate calculations of reverberation traveltimes.

Keywords: Composition and structure of the mantle; Phase transitions; North America; Body waves; Computational seismology.

1. Introduction

Recordings of long-period (T > 10 s) shear waves are useful data to map seismic discontinuities and velocity gradients in the mantle transition zone (MTZ) (e.g., Shearer, 1990). The mineral-phase transitions near depths of 410 and 660 km produce the highest amplitude shear-wave reflections from the mantle after the ScS wave arrival (e.g., Shearer & Buehler, 2019), before the SS arrival (e.g., Flanagan & Shearer, 1998), and between multiple ScS reflections (e.g., Revenaugh & Jordan, 1991) in stacks of transverse-component seismograms. We call these boundaries the "410-km discontinuity" and "660-km discontinuity" in this paper and define the MTZ as the layer of the mantle between the 410-km and 660-km discontinuities. The depths of the 410-km and the 660-km discontinuities and the thickness of the MTZ constrain the temperature and composition of the mantle (e.g., Bina & Hellfrich, 1994; Xu et al. 2008) and heat and mass transfer between the upper and lower mantle.

Most seismological studies of hundreds to thousands of waveforms are based on 1-D seismic reference profiles and ray theory to facilitate the analysis and computations. However, long-period shear waves are sensitive to seismic inhomogeneities in the mantle beyond the geometric ray so ray-theoretical calculations of traveltimes and waveform shifts may be inaccurate (e.g., Tromp et al. 2005). Modeling inaccuracies have been discussed thoroughly for the SS wave and its precursors (e.g., Neele et al. 1997; Zhao & Chevrot, 2003; Bai et al. 2012; Guo & Zhou, 2020; Koroni & Trampert, 2016, 2021), but they exist for all long-period seismic wave reflections and

conversions in the MTZ, including the multiple ScS reverberations (e.g., Haugland et al. 2020) and receiver functions (e.g., Deng & Zhou, 2015).

The receiver-side shear-wave reverberation in the upper mantle is the phase of interest in this paper. It has been introduced by Shearer & Buehler (2019), a study we abbreviate as SB19 from hereon, as a new wave type for probing the upper mantle and the MTZ. Using USArray waveforms and a common-reflection-point (CRP) imaging method, SB19 estimated the depths of the 410-km and 660-km discontinuities to be 40–50 km deeper beneath the western US than beneath the central and eastern US. This is an important study outcome as it implies that the seismic contrast in the upper mantle beneath the tectonically active western US and tectonically stable central and eastern US extends into the MTZ.

SB19 used ray theory and the 1-D iasp91 velocity model to relate traveltimes to reflector depths. They acknowledged that 3-D seismic velocity heterogeneity may have a significant effect on the amplitude, coherence, and depths of the 410-km and the 660-km discontinuities in the CRP images. In this paper, we follow up on their recommendation to investigate how 3-D velocity structure changes the interpretation of CRP imaging results and to test the hypothesis that the 410-km and 660-km discontinuities beneath the US are unperturbed. In Section 2, we confirm that the 410-km and 660-km discontinuities are 40–50 km deeper beneath the western US than the central-eastern US if the traveltime analysis is based on a 1-D reference structure. In Section 3, we explore how strongly 3-D shear-velocity inhomogeneities, as constrained by shear-wave velocity tomography, perturb reverberation traveltimes and how ray-theoretical traveltime corrections change the CRP images. In Section 4, we use spectral-element method seismograms to evaluate the accuracy of ray

theory in predicting the reverberation traveltimes and whether undulations on the 410-km and 660-km discontinuities are resolvable by long-period shear wave reflections (section 4). In section 5, we discuss our key findings.

2. Mapping the 410-km and 660-km discontinuities by 1-D common reflection point imaging

2.1 The Ssds phase

A shear-wave reverberation beneath the receiver is abbreviated here as "Ssds", following the notation of SB19. Ssds is a shear wave that follows a similar path in the mantle as the direct S wave and reflects off the free surface and off the top of a reflector at depth d before it is recorded by a seismometer on the surface (Figure 1). The arrival time of Ssds after S depends primarily on d and the shear-wave speed above the reflecting layer. For PREM (Dziewonski & Anderson, 1981), an earthquake at the surface, and an epicentral distance of 80°, Ss410s and Ss660s arrive 159.6 s and 242.2 s after S, respectively. Ssds can interfere with SS precursors but the two phases have different slownesses and are distinguishable in waveforms recorded over a wide epicentral distance range. The top-side reflection sdsS near the source has the same traveltime as Ssds at any distance for a 1-D velocity structure (Figure 1). For stations at similar azimuths, source-side reflection points are virtually identical whereas the Ssds reflection points are separated beneath the arrays of stations. Therefore, variations in the Ssds traveltime are primarily due to seismic structure in the upper mantle beneath the seismic stations. There is no source-side and receiver-side

ambiguity if the analysis is limited to earthquakes deeper than the reflecting boundaries of interest (Liu & Shearer, 2021) but the data set would be significantly smaller.

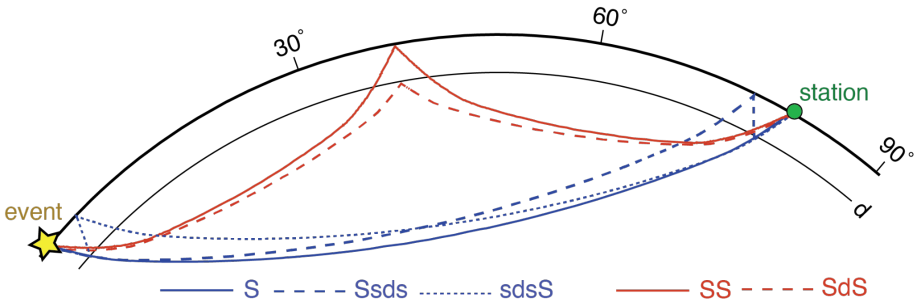

Figure 1. Ray diagram of the phases S (solid blue line), Ssds (dashed blue line), sdsS (dotted blue line), SS (solid red line) and the SS precursor SdS (dashed red line) for an epicentral distance of 80 degrees.

2.2 USArray waveforms

To confirm SB19's imaging results, we analyze 59,517 transverse-component displacement waveforms from 337 global earthquakes (Figure 2) recorded by stations from the USArray and other regional networks in the forty-eight conterminous United States. The earthquakes are shallower than 35 km, so the direct S wave and the depth phase sS form a single pulse at long periods. The earthquakes have moment magnitudes smaller than 7.0 so rupture complexity does not affect long-period waveforms strongly. The epicentral distances are between 60° and 110° and waveforms have been filtered using a bandpass Butterworth filter with corner frequencies of 20 mHz and 80 mHz. We align the waveforms on the peak S-wave displacement and normalize them, so the S waves have the same polarities and maximum displacements of +1. In all waveforms, the S-wave displacement is at least six times larger than the signal in the 100-second window prior to the S wave onset. The maximum and the root-mean-square displacement in the window [30 s, 220 s] after the S-wave arrival time are more than six times and three times smaller than the peak S-

wave displacement, respectively. We remove earthquakes with fewer than 20 seismograms left after these quality control steps.

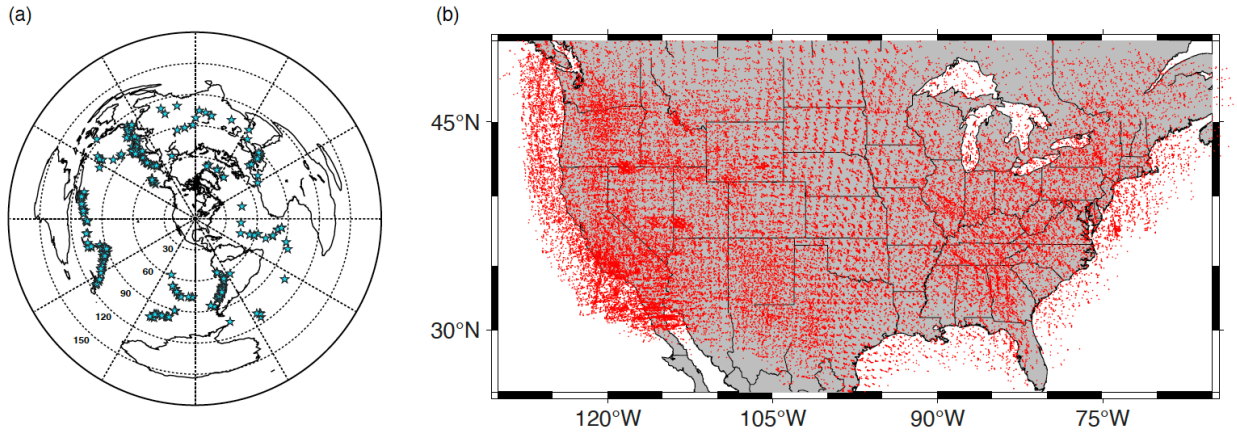

Figure 2. (a) Epicenters of earthquakes (stars) used in this study. The dashed circles have a common center of [40°N, -95°E] and radii of 30, 60, 90, 120, and 150 degrees. (b) Red dots show reflecting points of Ss410s at the 410-km discontinuity for the 59,517 seismograms in our data set.

A record section of the sum of these waveforms brings out Ss410s and Ss660s as the strongest mantle reflections (Figure 3). The Ss410s and Ss660s have mean amplitudes of about 0.05 and are recorded without interference with ScS and SS at distances larger than 60° and 75°, respectively. The SS precursors S410S and S660S are weaker than Ss410s and Ss660s at distances smaller than 110° (e.g., Shearer, 1991). Although we cannot rule out that signals labeled ‘A’ and ‘B’ in Figure 3a are side lobes due to the applied Butterworth filter, signal ‘A’ may be a SS-precursor reflection at a depth of about 125 km and signal ‘B’ may be a Ssds reflection from the lithosphere-asthenosphere boundary (LAB), a boundary that has also been studied with P-wave and S-wave receiver functions (Rychert et al. 2007; Abt et al. 2010; Hopper & Fischer, 2018) and multiple S-wave reflection (Liu & Shearer, 2021).

Ssds reflections from the uppermost lower mantle below the 660 arrive more than 250 s after S and do not interfere with SS and the S410S precursor at distances larger than 95° in region 'C' of Figure 3a. However, it is difficult to differentiate reflections below the 660 from shallower SS precursors because S waves are attenuated by diffraction around the core and the slowness resolution is poor. The high-amplitude signal about 330 s after S waves has a slowness of roughly 1.0 sec/degree which is smaller than the slowness of any SS precursor. Its traveltime is similar to that of the phase Ss410s410s (i.e., the shear-wave reverberation with two up-and-down shear-wave segments between the surface and the 410-km discontinuity) and the phase PSs660s (i.e., the PS phase with an additional top-side reflection off the 660-km discontinuity). However, it is unlikely that these phases can be recorded with high amplitudes on transverse component records.

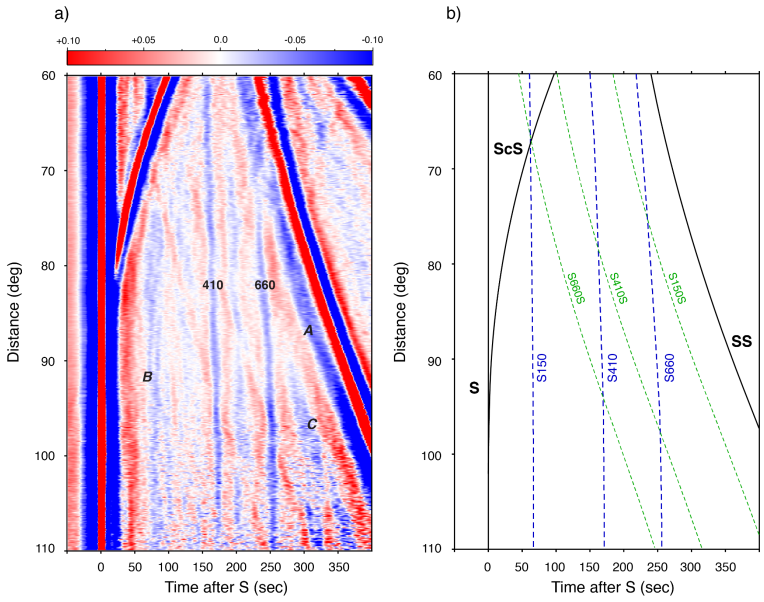

Figure 3. (a) Record section of transverse component seismograms used in this study. Shown is the amplitude of ground displacement in red and blue for positive and negative polarities, respectively, with a color intensity proportional to the absolute value. The seismograms have been aligned to the S wave at time 0. (b) The arrival times of S, ScS, and SS (black lines), S150, S410 and S660 (blue dashed lines), and the SS-precursors S150S, S410S and S660S (green dashed lines) have been computed for PREM for a source depth of 20 km.

174 **2.3 Common reflection point imaging**

175

176 By 1-D common reflection point (CRP) mapping, we convert the Ssds-S difference times to the
177 locations of the Ssds reflecting points in the upper 800 km of the mantle beneath the USArray. We
178 use the TauP software (Crotwell et al. 1999) and the PREM velocity structure to calculate Ssds
179 reflection points and traveltimes. At a depth d, 1,716 reflection points are uniformly distributed on
180 a 1° × 1° horizontal grid between 25°N and 50°N and between -130°E and -65°E. The horizontal
181 grids are separated by 5 km from 10 to 1,000 km, for a total of 199 depths. For a grid point X, we
182 select waveforms for which the Ssds reflection points are within the 1° × 1° bin around X and for
183 which the theoretical Ssds arrival time differs more than 15 s from the theoretical arrival times of
184 sS, ScS, and sScS, and more than 50 s from the arrival time of SS to avoid wave interference. If
185 fewer than five waveforms are available, we deem the mean displacement of Ssds to be
186 inaccurately determined.

187

188 Since we use shallow focus earthquakes, the source-side and the receiver-side reflections have
189 identical traveltimes. From synthetic seismograms for PREM, we have verified that they are
190 equally strong so we attribute half of the mean Ssds amplitude to a source-side reflection. To
191 construct the CRP images, we estimate source-side reflections of the 337 earthquakes and receiver-
192 side reflections for the 1,716 grid points sequentially following two steps. First, we determine the
193 mean of the Ssds displacement for each earthquake at the theoretical arrival time of Ssds. We
194 assume that the mean displacement source-side reflection has been amplified and that receiver-
195 side structures do not contribute coherent signals. Second, we subtract this mean value from the
196 Ssds displacement of each waveform, assuming that the residual displacement to be due to

197 coherent reflections beneath the USArray. We exclude events with fewer than 20 seismograms.
198 After mapping the Ssds signals onto the grid ray theoretically, we average the receiver-side
199 reflection amplitudes with 1°x1° bins, which are narrower than the Fresnel zones of 10-s period
200 Ssds reflections in the mantle transition zone, as shown by SB19. We have also implemented the
201 approach by SB19, who estimates the source-side and receiver-side contributions to Ssds in one
202 step using a sparse-matrix inversion solver. This approach yields smaller amplitudes of the Ssds
203 reflections but the overall character of the CRP image, including the depths of the 410-km and
204 660-km discontinuities, are similar (Supplementary Figure S1).

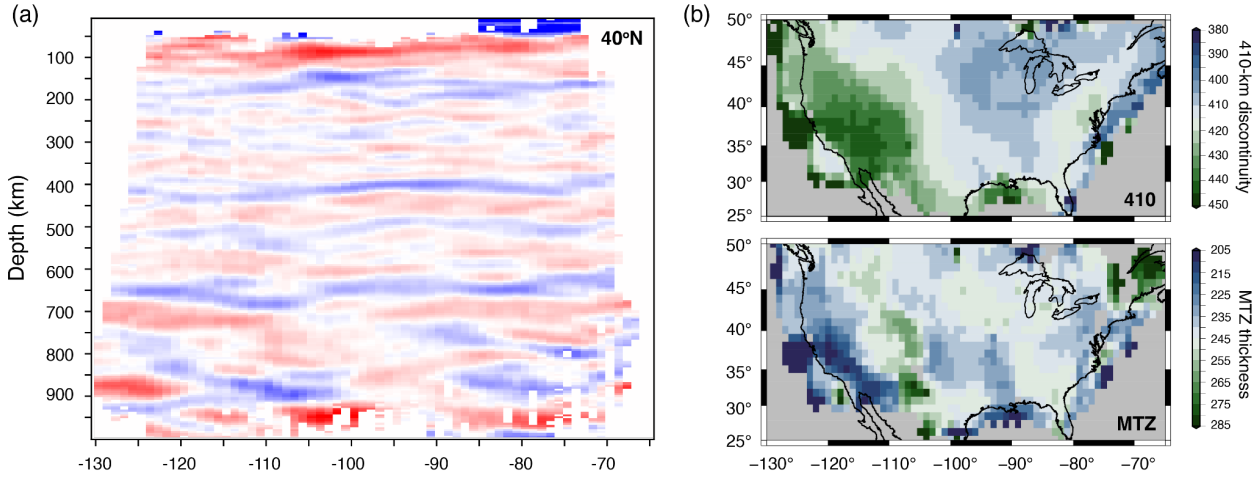

205

206 **Figure 4.** (a) Vertical section of the CRP image along 40°N. Blue and red colors indicate reflectors with positive and
207 negative impedance contrasts, respectively. The color intensity is highest when the impedance contrast is strongest.
208 All record section profiles use this color scale. (b) Depth of the 410-km discontinuity (top) and the thickness of the
209 mantle transition zone (bottom).

210

211 Figure 4a shows a vertical section of the CRP image along the 40°N parallel. As expected from
212 Figure 3, the 410-km and 660-km discontinuities are the clearest reflectors. Variations of the
213 Ss410s-S and Ss660s-S difference times project as spatial variations in the depth of 410-km and
214 660-km discontinuities. The 410-km and 660-km discontinuities are deeper and more complex

beneath the western US (west of -100°E) than beneath the central and eastern US. This is also apparent in other sections through the CRP images shown in Supplementary Figure S4. The 410-km discontinuity is strongest between longitudes -100°E and -75°E. The 520-km discontinuity may be responsible for a relatively weak Ssds reflection between the 410-km and 660-km discontinuities. The CRP images near the 410-km and 660-km discontinuities west of -100°E are complex, which was also noted by SB19. Strong reflectors corresponding to the Ssds signals in region B of the record section of Figure 3 are mapped at about 100 km and 150 km depth, but their depths and strengths vary. The incoherent structures at depths larger than 800 km are most likely imaging artifacts because these structures correspond to the amplified signals in region C of Figure 3, where S are diffracting waves and the slowness resolution is relatively poor.

Figure 4b shows maps of the depth of the 410-km discontinuity and the thickness of the MTZ. These are estimated from the absolute minimum values of the mean displacements in the CRP image in the depth ranges of 350–470 km (for the 410-km discontinuity) and 620–730 km (for the 660-km discontinuity) by cubic spline interpolation. We do not estimate the depth of the 410-km and 660-km discontinuities where a secondary absolute minimum is stronger than 40% of the absolute minimum in these depth ranges. The depth of the 410-km discontinuity varies by 40–50 km. The 410-km discontinuity is deepest beneath the southern Basin and Range and the Colorado Plateau and shallowest beneath the central plains and the Atlantic coast. The thickness of the MTZ varies less than 10 km because the 410-km and 660-km discontinuities depth variations are similar. The MTZ is thinnest beneath California and thickest beneath the Southern Rocky Mountains and the Colorado plateau. The MTZ thickness is anomalous in small regions near the margins of our model domain. This includes the extremely thin (210 km) MTZ beneath the west coast of central

California which was also resolved by SB19. However, the CRP images have low resolution here because the data coverage is poor.

SB19 resolved similar maps as Figure 4b, indicating that our and SB19's data sets contain consistent variations of the Ss410s-S and Ss660s-S difference times and that estimates of the depths of the 410-km and 660-km discontinuity do not strongly depend on the applied mapping method.

The S410S and S660S precursors interfere with the reverberations (Figure 3). To test their influence, we compare CRP images with and without seismograms for which the reflecting time falls within 50 s of either of the precursors (Supplementary Figure S6). The maps of the depth of the 410-km discontinuity and the MTZ thickness are similar so interference with precursors has a minor effect on the imaging results. The large difference near the Pacific coast is due to lack of data coverage.

3. Influence of 3-D seismic heterogeneity on the CRP images

The map of the depth of the 410-km discontinuity shown in Figure 4b is reminiscent of the estimated shear-wave velocity variations in the upper mantle beneath the US from the modeling of regional S-waves (e.g., Grand & Helmberger, 1984), surface-waves (e.g., Van der Lee & Nolet, 1997), and, more recently, ambient noise (e.g., Bensen et al. 2008), P-wave polarization (Park et al. 2019) and surface-wave amplification (Eddy & Ekström, 2014; Bowden & Tsai, 2017). This indicates strongly that shear-velocity variations in the mantle affect Ss410s-S and Ss660s-S

difference times and that a mapping method based on a 1-D velocity structure would overestimate undulations of the 410-km and 660-km discontinuities.

3.1 S-wave traveltime variations

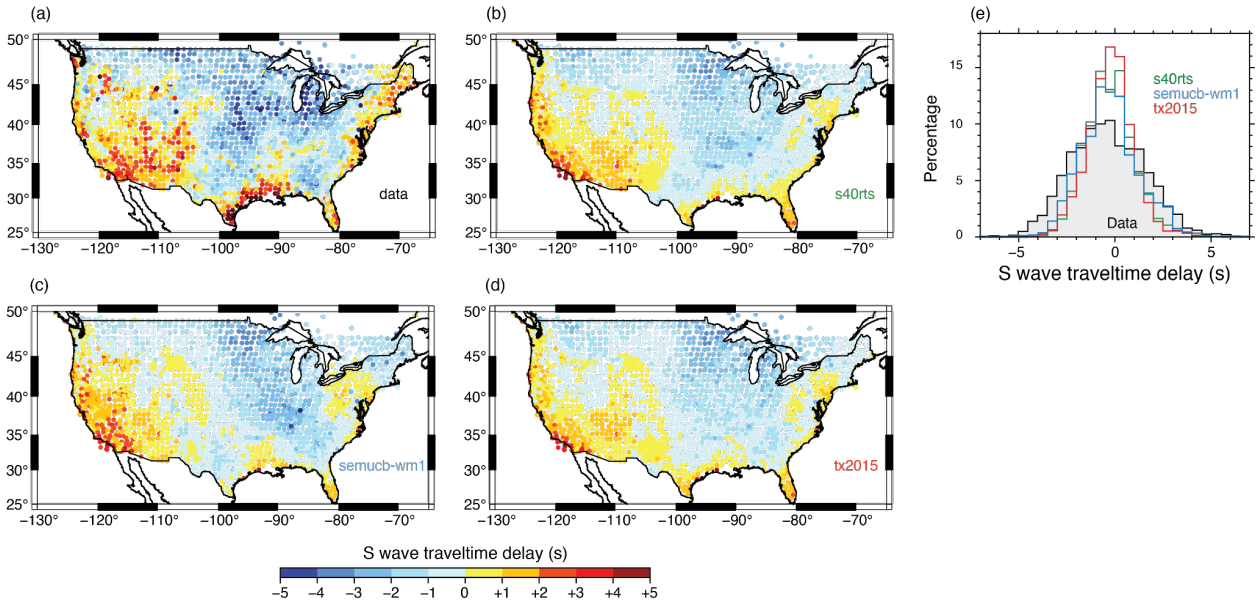

Figure 5. The recorded (a) and predicted (b, c, d) traveltime delays of S waves by tomographic mantle models S40RTS (in b), SEMUCB-WM1 (in c), and TX2015 (in d) with crustal model CRUST1.0. Each circle indicates the location of a seismic station. Its color indicates the mean of the S-wave traveltime delays with respect to the PREM model for at least five S waves. (e) Histograms of the S wave traveltime delay in the data (gray fill) and predictions by S40RTS (green line), SEMUCB-WM1 (blue line), and TX2015 (red line) for the stations in panels a–d.

Figure 5a shows how shear-wave velocity variations in the crust using CRUST1.0 (Laske et al. 2013) and in the upper mantle affect the traveltimes of S waves. Plotted are the average S-wave delay with respect to the PREM velocity model of at least five S-waves recorded at seismic stations from the USArray. The delay times have been corrected for 'source terms', representing the effects of a potential mislocation of the earthquake location and origin time on the absolute S wave

278 traveltime. S waves recorded by USArray stations in the western US (the tectonically active
279 region) arrive on average 5–6 seconds later than at stations in the central and eastern US (the stable
280 platform). The global-scale mantle models S40RTS (Ritsema et al. 2011), SEMUCB-WM1
281 (French & Romanowicz, 2014), and TX2015 (Lu & Grand, 2016) predict a similar traveltime
282 pattern (Figures 5b–d) but the range is slightly smaller than in the data (Figures 5e). Our
283 calculations indicate that the crustal structure from CRUST1.0 enhances the east-west contrast
284 only slightly, so wave speed variations in the mantle are primarily responsible for the S-wave
285 traveltime differences.
286
287 The imperfect match between the recorded and the predicted S wave traveltime is expected because
288 tomographic models do not perfectly explain the recorded traveltime variation of any shear wave
289 (e.g., Ritsema et al. 2004). Nevertheless, it is obvious that shear-velocity heterogeneity affects
290 teleseismic S wave traveltimes across the USArray. Since Ssds has two additional propagation
291 legs through the upper mantle, the Ss410s-S and Ss660s-S difference times are likely to be double
292 the variation shown in Figure 5a due to shear velocity heterogeneity only. If shear-wave speed
293 variations in the upper mantle beneath North America are ignored in the modeling, a variation of
294 the Ss410s-S and Ss660s-S difference times of more than 10 s would imply that the depths of the
295 410-km and 660-km discontinuities vary by about 18 and 20 km or more. This is of the same
296 magnitude as resolved in Figure 4.
297
298 **3.2 Ray-theoretical corrections**
299

Since the tomographically predicted S-wave traveltime variation of 5–6 seconds across the USArray is a significant fraction of the recorded traveltime variation, we suspect that shear-velocity variations in the upper mantle influence the CRP imaging and our estimate of the depth of the 410-km discontinuity. To quantify this, we determine the CRP image for "corrected" Ssds-S difference times. From the measured Ssds-S difference time, we subtract the predicted difference time anomaly (positive or negative) by shifting the waveform around the theoretical Ssds arrival time. We predict the Ssds-S difference time by ray tracing through tomographic model S40RTS for the mantle and CRUST1.0 for the crust. The Ssds-S difference time predictions are similar for SEMUCB-WM1 and TX2015, as expected from Figure 5.

Figure 6a shows the CRP image along the 40°N parallel after traveltime corrections. The character of the corrected (Figure 6) and uncorrected (Figure 4) CRP images are the same, but the 410-km and 660-km discontinuities are flatter boundaries across the USArray. This is especially clear for the region between -100°E and -80°E where the 410-km and 660-km discontinuities are relatively simple. Figure 6b emphasizes that the depth variation of the 410-km discontinuity is much smaller when the CRP image is based on tomographically corrected Ssds-S difference times. The 410-km discontinuity is not deeper in the west than in the east. The thickness of the MTZ in the corrected and uncorrected images are similar because shear-velocity variations are relatively weak in the MTZ compared to the uppermost mantle. The histograms shown in Figures 6c illustrate that the depth variation of the 410-km discontinuity is about a factor of two smaller when traveltime corrections have been applied to the data and that the corrections do not change the range in MTZ thickness values. The traveltime corrections change the mean depth of the 410-km and 660-km

discontinuities by about 10 km, which is similar to the change obtained by Shearer & Buehler (2019) using ray-theoretical corrections computed for a regional 3-D velocity model.

The ray-theoretically corrected images may not reflect the actual depth variations of the 410-km discontinuity. Since S40RTS and any other tomographic model does not perfectly explain the recorded S-wave traveltime variation (see Figure 3), it is unlikely that the traveltime corrections have completely removed the effects of the shear-velocity structure on the CRP image. Further, we show in the next section that ray-theoretical predictions of long-period Ssds-S traveltimes are inaccurate and that corrections can project as spurious signals in the CRP images.

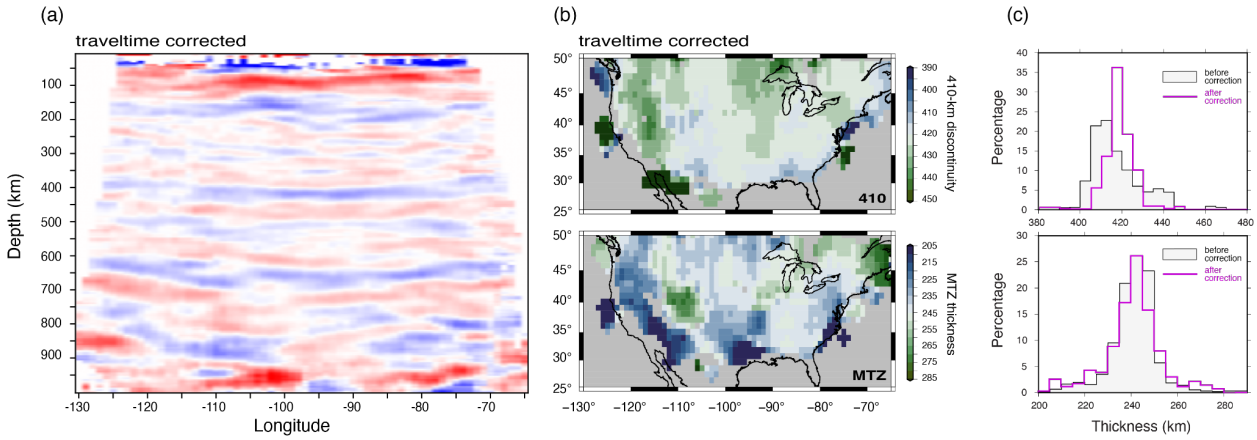

Figure 6. Depth of the 410-km discontinuity (in a) and the thickness of the transition zone (in b) estimated after ray-theoretical traveltime corrections have been applied. The color scale in a is the same as Figure 4a. Panels c and d show histograms of the resolved depth of the 410-km discontinuity and the thickness of the MTZ beneath the USArray with (black line) and without (purple line) traveltime corrections. Compare with Figure 4b.

4. Resolution tests using spectral-element-method waveforms

We analyze synthetic waveforms to test the robustness of our CRP imaging approach, the resolution of 410-km and 660-km discontinuities undulations from long-period Ssds waveform data, and the accuracy of ray-theoretical corrections. The waveforms are computed using the SPECFEM3D-Globe software (e.g., Komatitsch & Tromp, 2002; Komatitsch et al. 2016) modified by us to allow for undulations of the 410-km and 660-km discontinuities. The eight test structures are PREM, S40RTS (Figure 7a), SEMUCB-WM1, TX2015, and structures T2, T5, T8 (Figure 7b), and T5-410-S40. The simulations account for Earth's ellipticity and anelasticity using the Q structure of PREM. In each structure, the density and velocities in the uppermost mantle extend to the surface. We remove the crust from seismic models to suppress reverberations in the crust that complicate the waveforms following the S wave (Supplementary Figure S5).

The one-dimensional PREM structure with discontinuities at 220 km, 400 km, 670 km depth serves as a baseline model for determining artifacts in the CRP images unrelated to 3-D structure in the upper mantle. In our calculations, S40RTS, SEMUCB-WM1, and TX2015 represent models of the 3-D shear velocity structure in the mantle. We do not include the crustal structure, adopt PREM as the reference mantle structure for each of the three models, and assume the Voigt average shear-velocity variations in the anisotropic SEMUCB-WM1 model. The 220-km, 410-km and 660-km discontinuities are horizontal boundaries at the same depths as in the PREM model. Models T2, T5, and T8 have the same layered velocity structure as PREM but the 410-km and the 660-km discontinuities are sinusoidal boundaries with amplitudes of 15 km and wavelengths of 2°, 5°, and 8°, respectively. The undulations of the 410-km and 660-km discontinuities are oppositely directed so the thickness of the MTZ varies up to 30 km with respect to the average of 270 km. The model T5-410-S40 has the 3-D shear velocity structure of S40RTS and sinusoidal undulations of the 410-

363 km discontinuity with a wavelength of 5°. The 660-km discontinuity is a horizontal boundary in
364 T5-410-S40.
365

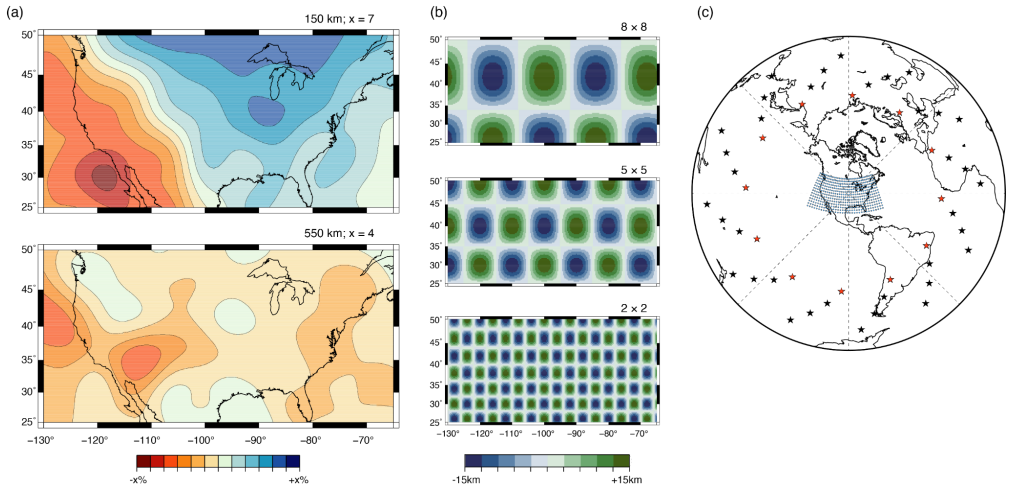

366

367 **Figure 7**. (a) Maps of the shear-velocity variation at (top) 150 km and (bottom) 500 km depth according to S40RTS.
368 The east-west contrast across the US is similar for SEMUCB-WM1 and TX2015. (b) Harmonic undulations of the
369 410-km and 660-km discontinuities for (from top to bottom) models T8, T5, and T2 with spatial wavelengths of 8°,
370 5°, and 2°. (c) Distribution of hypothetical earthquakes (stars) and stations (circles). For models PREM, S40RTS, T8
371 and T5 we compute waveforms for the twelve earthquakes indicated by red stars. For T2, we compute waveforms for
372 these earthquakes and the additional 36 earthquakes indicated by black stars.
373

374 For each of the eight structures, we compute waveforms at periods longer than 10 s for 462 stations
375 in a rectangular 2° × 2° grid between longitudes 130°–65°W and latitudes 25°–50°N (Figure 7c).
376 We calculate waveforms for 12 earthquakes uniformly distributed at a distance of 75° from [-
377 100°E, 40°N]. We use 48 earthquakes distributed in a spiral for structure T2. All earthquakes have
378 the same dip-slip source mechanism (source parameters for event 080596G in the Global CMT
379 catalog) to ensure strong radiation of SH waves to teleseismic stations. The uniform data coverage
380 is sufficient to investigate the effects of velocity heterogeneity on Ssds-S traveltimes and the

resolution of undulations of the 410-km and 660-km discontinuities using long-period Ssds reflections. Because of the high computational cost, we cannot afford to reproduce the source-station combinations in the data and, therefore, we cannot estimate CRP mapping artifacts due to inhomogeneous slowness and azimuthal sampling.

4.1 Testing ray-theoretical traveltime corrections

Figure 8 shows the CRP images along the 35°N parallel in the central region of the model domain determined for the PREM and S40RTS models. Supplementary Figure S2 shows similar CRP images for SEMUCB-WM1 and TX2015. The CRP image for PREM in Figure 8a is the ideal case as the assumed velocity structure of the mantle is identical to the structure used to calculate traveltimes and ray paths. Artifacts are entirely due to the implementation of the CRP mapping procedure, the limited frequency band of the waveforms, and wave interference. PREM's velocity discontinuities at 220, 400, and 670 km depth are resolved about 10 km shallower in the mantle because the crust is not included in the waveform computations. Since the waveforms are computed for periods longer than 10 s and since shear wave speed increases with depth, reflectors at larger depths are more stretched than at shallower depths. The imaged 660-km discontinuity is therefore only about 60% stronger than the imaged 410-km discontinuity even though the impedance contrast at the 660 is a factor of two stronger than at the 410-km discontinuity. The CRP image derived from PREM waveforms is mostly free of artificial layering between 150 km and 750 km depth. The side lobes of the 660 near -65°E are artifacts near the boundaries of the station grid. Layering near 100 km depth, which is especially strong near the center of the CRP image, shows that the Ssds reverberation is not an ideal wave type for imaging the uppermost

mantle. The arch-shaped structure below 750 km depth is likely the projection of shallow SS precursors misinterpreted as Ssds reflections deep in the transition zone as discussed in section 2.1.

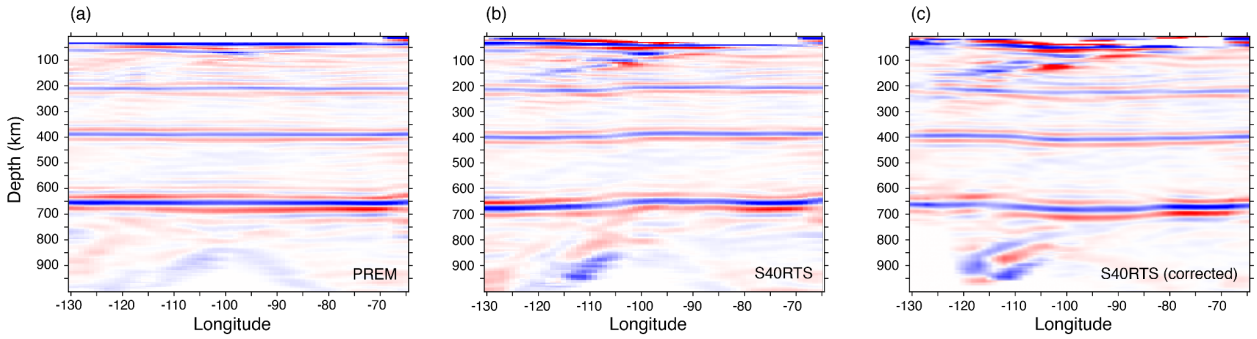

Figure 8. CRP images along the 35°N parallel determined for (a) PREM synthetics, (b) S40RTS synthetics, and (c) S40RTS synthetics after ray-theoretical corrections have been applied. The color scale is the same as Figure 4a.

The CRP image derived from S40RTS waveforms is more complex (Figure 8b). The 410-km and 660-km discontinuities deepen from east to west because S40RTS predicts that Ssds traveltimes through the upper mantle are shorter beneath the central and eastern US than beneath the western US and we use the PREM velocity structure to convert traveltimes to reflector depths. The velocity heterogeneity in S40RTS causes misalignments of Ssds signals and therefore fluctuations in the strength of the 410-km and the 660-km discontinuities from west to east by up to a factor of two. For example, the 660 appears as a relatively weak reflecting boundary between longitudes -120°E and -110°E, near the transition between the low-velocity upper mantle of the western US and the high-velocity upper mantle beneath the central US. In addition, spurious reflectors are particularly strong between -120°E and -100°E, where horizontal gradients in the uppermost mantle are strongest. It is difficult to identify how complex wave propagation produced the complexity in the CRP image, but the CRP image based on USArray waveforms is also most complex for the western

US, and a tilted reflective structure in the upper mantle has been observed by SB19 in their data image, albeit with an eastward dip and a greater depth extent.

Figure 8c shows the CRP image based on the S40RTS synthetics after applying ray-theoretical traveltime corrections following the procedure outlined in section 4.3. The traveltime corrections do not remove, and may even amplify the CRP image artifacts for depths shallower than 100 km and deeper than 750 km. More significantly, the ray-theoretical calculations appear to overpredict the contribution of shear-velocity heterogeneity to the Ss410s-S and Ss660s-S traveltime differences. After traveltime corrections, the 410-km and 660-km discontinuities are projected shallower beneath the western US than the central US, opposite to the imaged depths of the 410-km and 660-km discontinuities prior to corrections.

The inaccuracy of ray theory in predicting the shear-wave traveltime perturbations is illustrated further in Figure 9. It shows the estimated depths of the 410-km discontinuity and the thickness of the MTZ based on the 1-D CRP method applied to synthetic waveforms computed for S40RTS. Supplementary Figure S3 shows that we obtain similar results for SEMUCB-WM1 and TX2015. The total variation in the depths of the 410-km discontinuity is about 15–20 km. As expected, the depth of the 410-km discontinuity (Figure 9a) mimics the shear-velocity variations in the upper mantle of S40RTS (Figure 7a) and the S-wave traveltime delay map shown in Figure 5. Variations in the thickness of the MTZ (Figure 9b) of about 10 km are small compared to the depth variations of the 410-km and 660-km discontinuities because shear velocity variations in the MTZ are much weaker than in the uppermost mantle.

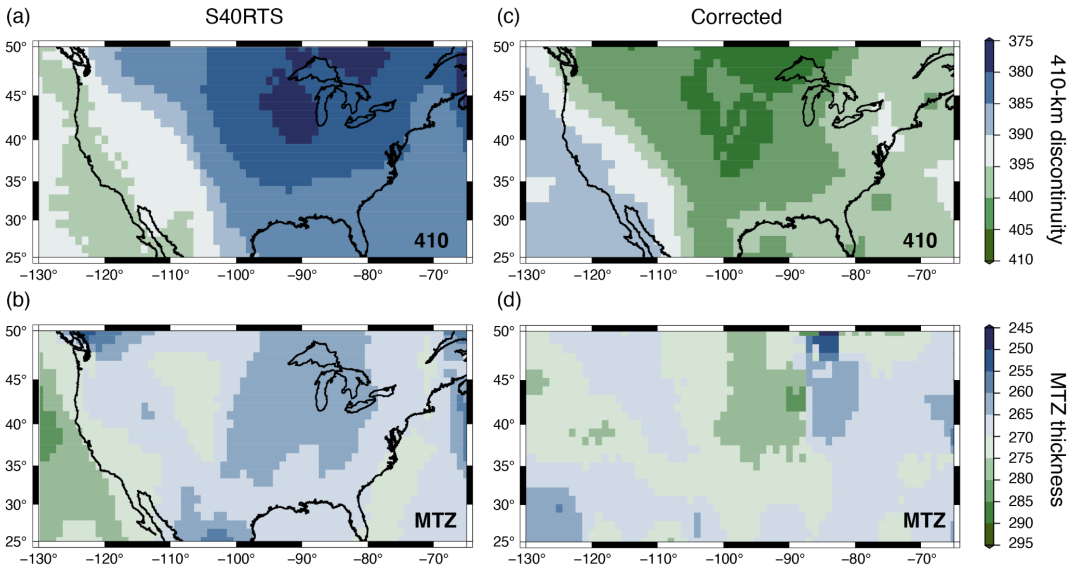

Figure 9. Depths of the 410-km discontinuity (top row) and the thicknesses of the transition zone (bottom row). Panels (a) and (b) are estimated from spectral-element-method seismograms calculated for model S40RTS. Panels (c) and (d) show the same estimates after ray-theoretical corrections have been applied to the waveforms.

If ray-theoretical traveltime corrections are precise, we must expect that the CRP images of the ray-theoretical corrected S40RTS, SEMUCB-WM1, and TX2015 waveforms are similar to the CRP image for the PREM model because the 410-km and 660-km discontinuities are horizontal boundaries in all models. However, we find this not to be the case. While the elevation of the 410-km and 660-km discontinuities beneath the western US (by 10 and 11 km, respectively) and their depressions beneath the central-eastern US (by 11 and 12 km, respectively) have the expected trends, the corrections are larger than expected ray-theoretically. In the corrected image, the 410-km discontinuity is shallower in the western US than in the eastern US (Figure 9c) opposite to the uncorrected CRP image (Figure 9a). In the western US, the inferred and predicted depth correction differ by a factor of 1.7. The MTZ thickness has a smaller variation than the depth of the 410-km discontinuity (Figure 9c and 9d). After corrections, a larger area has a thickness within 265-275

461 km. The corrected Pacific coast changes from thicker to slightly thinner than the surrounding area,
462 and the central US has the largest thickening by about 15 km.
463
464 **4.2 The resolution of undulations on the 410-km and 660-km discontinuities**
465
466 Figure 10 shows the depths of the 410-km and the 660-km discontinuities and the thickness of the
467 MTZ resolved for models T2, T5, and T8. The checkerboard pattern of the undulations on the 410-
468 km and 660-km discontinuities are resolved for T5 and T8 but the amplitude of the undulations is
469 underestimated. The resolved thickness of the MTZ varies, on average, 12 km and 6 km less than
470 in the original T8 and T5 models. The resolution of the undulations in T2 is poor despite using a
471 larger set of waveforms for 48 earthquakes. From experiments, we have found that the resolution
472 does not improve if we densify the grid of stations to a 1-degree spacing. Therefore, fluctuations
473 of the depth of the 410-km or 660-km discontinuities with a wavelength of about 200 km are
474 intrinsically unresolvable from long-period Ssds waveforms because the Fresnel zone of Ss410s
475 and Ss660s in the upper mantle at the dominant frequency of about 0.05 Hz is about 500 km, much
476 wider than the undulations of the 410-km and 660-km discontinuities in T2.
477

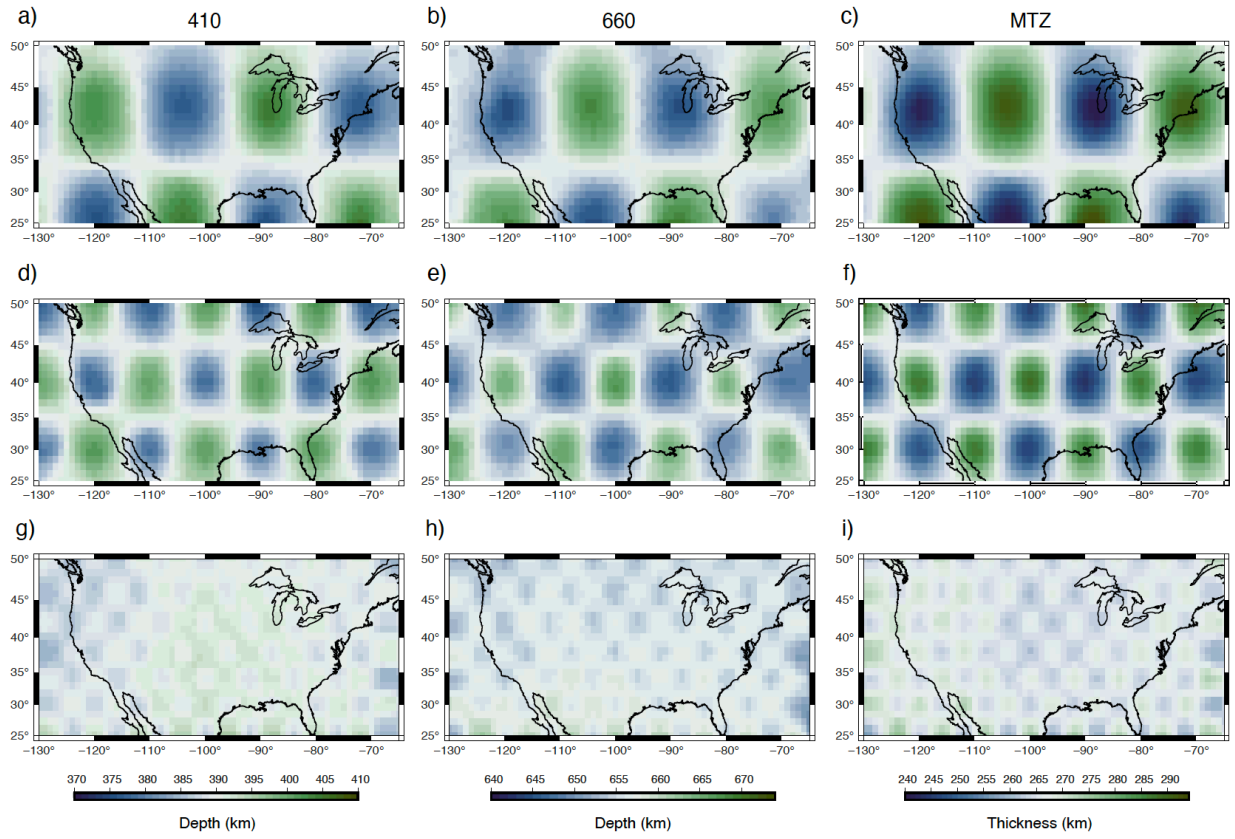

Figure 10. Depth maps of the 410-km, 660-km discontinuities, and MTZ thickness using the CRP imaging method for 8° × 8° (a, b, c) , 5° × 5° (d, e, f), and 2° × 2° (g, h, l) input topography models.

Figure 11 explores how undulations on the 410-km discontinuity would be resolved if they are embedded in 3-D velocity heterogeneity. We analyze waveform simulations for model T5-410-S40, described above. Figure 11 shows the resolved depth variation of the 410-km and the 660-km discontinuities and the MTZ thickness before (in a, c, and e) and after (in b, d, and f) ray-theoretical traveltime corrections have been applied to remove the effects of shear-velocity heterogeneity on the traveltimes. Figure 11a and 11b show that without traveltime corrections for 3-D heterogeneity, the resolved harmonic undulations of the 410 are overprinted by an east-to-west deepening. The ray-theoretical traveltime corrections remove the regional trend but the traveltime corrections do not accurately remove the effects of shear-velocity heterogeneity because

the depth variations of the 410-km discontinuity are not perfectly resolved (compare Figures 11b and 10d). The 660-km discontinuity. a horizontal boundary in T5-410-S40, is resolved with the same east-to-west deepening without traveltime correction. After traveltime corrections, the 660-km discontinuity does not have a distinct harmonic or tectonic structure but the topography indicates that the corrections are imperfect or that the effects of the 410-km discontinuity on the traveltimes may be projected as spurious 660-km discontinuity structures. As shown also in Figure 9, the ray-theoretical corrections are too strong, but smaller than a factor of two (Figure 9). The map of MTZ thickness, with a distorted checkerboard pattern, remains largely unchanged before and after the traveltime correction, though the checkerboard depth ranges become larger. The synthetic test of the joint effect of 3D mantle structure and undulations on the 410-km discontinuity suggests that the MTZ thickness can be determined more robustly than the absolute depths of 410-km and 660-km discontinuities using the CRP imaging approach.

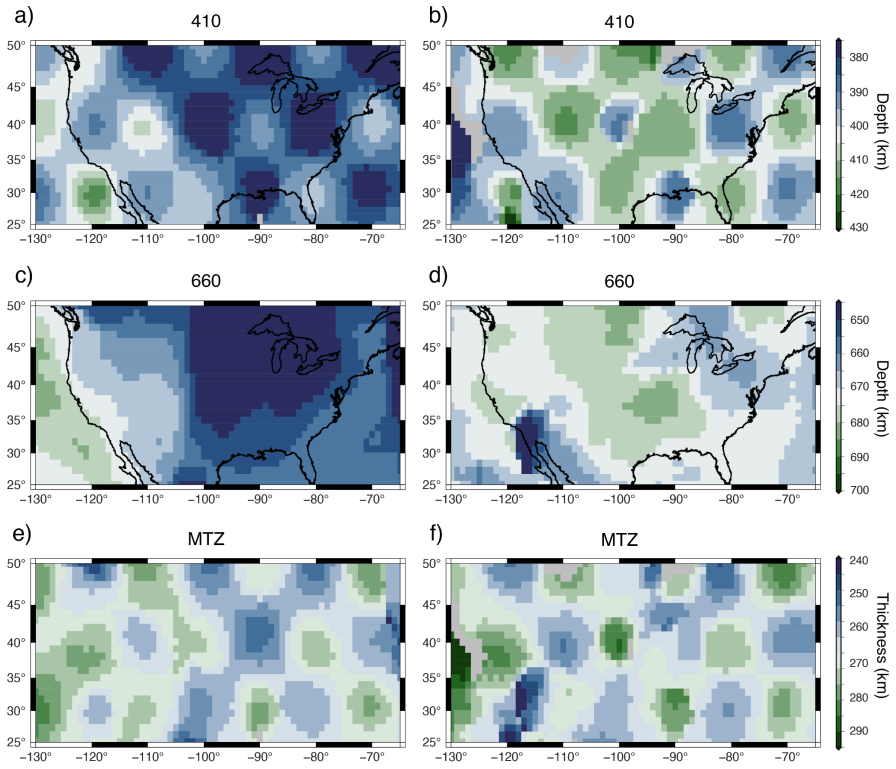

Figure 11. Maps of the 410-km (a and b) and 660-km (c and d) discontinuities, and the thickness of the MTZ (e and f) inferred for a model with the S40RTS model velocity structure for the mantle and 5x5 harmonic undulations on the 410. In the maps along the right column (b, d, f) the effects of the velocity structure have been removed by using ray-theoretical traveltime corrections.

5. Discussion and conclusions

The receiver-side S wave reverberation, denoted as Ssds, is a useful data type to map the shear velocity structure in the upper mantle, including undulations of the 410-km and 660-km discontinuities of mineral phase transitions. Ssds complements SS precursor and P-to-S wave conversion (i.e., receiver function) imaging of the mantle because of its unique wave path geometry. In agreement with the analysis by SB19, we observe in record sections of waveform stacks that the Ss410s-S and Ss660s traveltime differences vary by up to 10 s across stations from the USArray. If the traveltime differences are attributed entirely to undulations on the 410-km and 660-km discontinuities, it implies that the 410-km and 660-km discontinuities are 40–50 km deeper beneath the western US than the central and eastern US. In turn, this would mean that the contrast between the tectonically active western US and the stable central and eastern US persists as a temperature or compositional contrast in the mantle transition zone and that there is a link between uppermost mantle and mantle transition zone dynamics.

However, the correlation between the resolved depth of the 410-km discontinuity (and the 660-km discontinuity) and tomographic maps of the shear-velocity structure in the upper mantle is high. This indicates that velocity heterogeneity in the uppermost mantle contributes significantly to the Ss410s-S and Ss660s-S traveltimes and the spatial variations of the depth of the 410-km

discontinuity inferred from CRP imaging. Ray-theoretical corrections of traveltimes for velocity heterogeneity by shifting segments of the waveforms containing Ss410s and Ss660s prior to CRP stacking reduce the variation in the depth of the 410-km discontinuity by a factor of two.

For at least two reasons we find ray-theoretical corrections imprecise. First, seismic tomography has uncertainties. Global models S40RTS, SEMUCB-WM1, and TX2015 agree on the east–west contrast but disagree on the magnitude of the traveltime perturbations (see Figure 4). Each model underestimates the S-wave traveltime delay at USArray stations (see Figure 5) which is consistent with the fact that tomographic models underestimate the magnitude of traveltime and waveform perturbations. Hence, the effect on the estimated depths of the 410-km and 660-km discontinuities depends on the chosen tomographic model. SB19 notes that the traveltime corrections may introduce incoherence in the CRP images and use that as a factor in determining the value of traveltime corrections.

Second, our experiments with spectral-element method synthetics demonstrate that ray-theoretical predictions of the Ss410s-S and Ss660s traveltime differences are inaccurate. CRP images derived from waveforms computed for a mantle with 3-D velocity heterogeneity and horizontal phase boundaries show the expected deepening of the 410-km and 660-km discontinuities below the western US and shallowing beneath the central and eastern US where the shear velocities are relatively low and high, respectively. After applying traveltime corrections for the 3-D wave speed structure, the 410 and 660 remain undulating boundaries. In fact, the 410-km and the 660-km discontinuities in the corrected CRP image are deeper beneath the central-eastern US than beneath the western US, opposite to the uncorrected CRP image. This indicates that ray theory overpredicts

the Ssds-S difference time by about a factor of two. This is the case for S40RTS, SEMUCB-WM1, and TX2015 and presumably also finer-scale regional tomographic models when finite-frequency effects are stronger. The inaccuracy of ray-theoretical predictions of the traveltime perturbations of long-period waves has been studied previously. For example, Neele et al. (1997) and Zhao & Chevrot (2003) have pointed out that for the broad SS sensitivity kernels at the reflection points on the surface or the mantle discontinuities. Bai et al. (2012) and Koroni & Trampert (2016) illustrate how the finite wave effects affect CRP images built from SS precursors similarly to the study here.

Finally, we note that the resolution of the depths of the 410-km and 660-km discontinuities depends on spatial scales of the undulations. Our experiments with spectral element method synthetics indicate that the Ssds-S traveltime difference is sensitive to 5° × 5° and 8° × 8° sinusoidal variations of the depths of the 410-km and 660-km discontinuities albeit that the height of the undulations is underestimated. Spatial variations of the 410-km and 660-km discontinuities on a 2° × 2° scale are not resolvable because such variations are smaller than the width of the Fresnel zone of Ssds at a period of 10 s.

Although it is beyond the scope of this work, it is better to simultaneously estimate the topography of the 410-km and 660-km discontinuities and shear velocity heterogeneity in the mantle of multiple data sets (e.g., Gu et al. 2003, Moulik and Ekström, 2014) using finite-frequency kernels that relate waveform perturbations to velocity heterogeneity and phase boundary topography (e.g., Guo & Zhou, 2020) or, preferably, using an adjoint tomography approach (Koroni & Trampert, 2021). Based on our experiments, the evidence for large-scale variations of the depth of the 410-

km discontinuity beneath the USArray is weak. As is well established, estimates of the thickness of the MTZ are not affected strongly by shear velocity heterogeneity. We find the thickness of the MTZ to vary by about 10 km, which is consistent with the receiver-function study of USArray data by Gao & Liu (2014) and much smaller than global variations of the MTZ observed in SS precursors studies (e.g., Flanagan & Shearer, 1998; Chambers et al. 2005).

Acknowledgments

This research was supported by the NSF (EAR-1644829). Data from the TA network was made freely available as part of the EarthScope USArray facility, operated by Incorporated Research Institutions for Seismology (IRIS) and supported by the National Science Foundation, under Cooperative Agreements EAR-1261681. The facilities of IRIS Data Services, and specifically the IRIS Data Management Center, were used for access to waveforms, related metadata, and/or derived products used in this study. IRIS Data Services are funded through the Seismological Facilities for the Advancement of Geoscience (SAGE) Award of the National Science Foundation under Cooperative Support Agreement EAR-1851048. The authors acknowledge the computing time provided on the AGUIA supercomputer supported by the HPC-STI (University of São Paulo). The SPECMFEM3D_Globe software was downloaded from the Computational Infrastructure for Geodynamics (https://geodynamics.org/). We thank the editor (Carl Tape) and two anonymous reviewers for their constructive comments.

Data availability

Information of selected 59,517 seismograms, 337 earthquakes, and source parameters of synthetic earthquakes, are deposited to the Deep Blue Data (https://doi.org/10.7302/napg-vt44).

References

Abt, D. L., Fischer, K. M., French, S. W., Ford, H. A., Yuan, H., & Romanowicz, B., 2010. North American lithospheric discontinuity structure imaged by Ps and Sp receiver functions. *Journal of Geophysical Research: Solid Earth*, *115*(B9).

Bai, L., Zhang, Y., & Ritsema, J., 2012. An analysis of SS precursors using spectral-element method seismograms. *Geophysical Journal International*, *188*(1), 293-300.

Bensen, G. D., Ritzwoller, M. H., & Shapiro, N. M., 2008. Broadband ambient noise surface wave tomography across the United States. *Journal of Geophysical Research: Solid Earth*, *113*(B5).

Bina, C. R., & Helffrich, G., 1994. Phase transition Clapeyron slopes and transition zone seismic discontinuity topography. *Journal of Geophysical Research: Solid Earth, 99*(B8), 15853-15860.

Bowden, D. C., & Tsai, V. C., 2017. Earthquake ground motion amplification for surface waves. *Geophysical Research Letters, 44*(1), 121-127.

Chambers, K., Woodhouse, J. H., & Deuss, A., 2005. Topography of the 410-km discontinuity from PP and SS precursors. *Earth and Planetary Science Letters, 235*(3-4), 610-622.

Crotwell, H. P., Owens, T. J., & Ritsema, J., 1999. The TauP Toolkit: Flexible seismic travel-time and ray-path utilities. *Seismological Research Letters*, *70*(2), 154-160.

Deng, K., & Zhou, Y., 2015. Wave diffraction and resolution of mantle transition zone discontinuities in receiver function imaging. *Geophysical Journal International, 201*(3), 2008-2025.

Dziewonski, A. M., & Anderson, D. L., 1981. Preliminary reference Earth model. *Physics of the earth and planetary interiors*, *25*(4), 297-356.

622 Eddy, C. L., & Ekström, G., 2014. Local amplification of Rayleigh waves in the continental United States observed
623 on the USArray. *Earth and Planetary Science Letters*, *402*, 50-57.

624 Flanagan, M. P., & Shearer, P. M., 1998. Global mapping of topography on transition zone velocity discontinuities by
625 stacking SS precursors. *Journal of Geophysical Research: Solid Earth, 103*(B2), 2673-2692.

626 French, S. W., & Romanowicz, B. A., 2014. Whole-mantle radially anisotropic shear velocity structure from spectral-
627 element waveform tomography. *Geophysical Journal International, 199*(3), 1303-1327.

628 Gao, S. S., & Liu, K. H., 2014. Mantle transition zone discontinuities beneath the contiguous United States. *Journal*
629 *of Geophysical Research: Solid Earth*, *119*(8), 6452-6468.

630 Grand, S. P., & Helmberger, D. V., 1984. Upper mantle shear structure of North America. *Geophysical Journal*
631 *International*, *76*(2), 399-438.

632 Gu, Y.J., Dziewoński, A.M. and Ekström, G., 2003. Simultaneous inversion for mantle shear velocity and topography
633 of transition zone discontinuities. *Geophysical Journal International, 154*(2), pp.559-583.

634 Guo, Z., & Zhou, Y., 2020. Finite-frequency imaging of the global 410-and 660-km discontinuities using SS
635 precursors. *Geophysical Journal International*, *220*(3), 1978-1994.

636 Haugland, S. M., Ritsema, J., Sun, D., Trampert, J., & Koroni, M., 2020. Common reflection point mapping of the
637 mantle transition zone using recorded and 3-D synthetic ScS reverberations. *Geophysical Journal International,*
638 *220*(1), 724-736.

639 Hopper, E., & Fischer, K. M., 2018. The changing face of the lithosphere-asthenosphere boundary: Imaging
640 continental scale patterns in upper mantle structure across the contiguous US with Sp converted waves.
641 *Geochemistry, Geophysics, Geosystems*, *19*(8), 2593-2614.

642 Komatitsch, D., & Tromp, J., 2002. Spectral-element simulations of global seismic wave propagation—I. Validation.
643 *Geophysical Journal International*, *149*(2), 390-412.

644 Komatitsch, D., Xie, Z., Bozdağ, E., Sales de Andrade, E., Peter, D., Liu, Q., & Tromp, J., 2016. Anelastic sensitivity
645 kernels with parsimonious storage for adjoint tomography and full waveform inversion. *Geophysical Journal*
646 *International*, *206*(3), 1467-1478.

Koroni, M., & Trampert, J., 2016. The effect of topography of upper-mantle discontinuities on SS precursors. *Geophysical Journal International, 204*(1), 667-681.

Koroni, M. and Trampert, J., 2021. Imaging global mantle discontinuities: a test using full-waveforms and adjoint kernels. *Geophysical Journal International, 226*(3), pp.1498-1516.

Laske, G., Masters, G., Ma, Z., & Pasyanos, M., 2013. Update on CRUST1. 0—A 1-degree global model of Earth's crust. In *Geophys. res. abstr*, vol. 15, p. 2658.

Liu, T., & Shearer, P. M., 2021. Complicated Lithospheric Structure Beneath the Contiguous US Revealed by Teleseismic S-Reflections. *Journal of Geophysical Research: Solid Earth*, *126*(5), e2020JB021624.

Lu, C., & Grand, S. P., 2016. The effect of subducting slabs in global shear wave tomography. *Geophysical Journal International, 205*(2), 1074-1085.

Moulik, P. and Ekström, G., 2014. An anisotropic shear velocity model of the Earth's mantle using normal modes, body waves, surface waves and long-period waveforms. *Geophysical Journal International, 199*(3), pp.1713-1738.

Neele, F., de Regt, H., & Van Decar, J., 1997. Gross errors in upper-mantle discontinuity topography from underside reflection data. *Geophysical Journal International, 129*(1), 194-204.

Park, S., Tsai, V. C., & Ishii, M., 2019. Frequency-dependent P wave polarization and its subwavelength near-surface depth sensitivity. *Geophysical Research Letters*, *46*(24), 14377-14384.

Revenaugh, J., & Jordan, T. H., 1991. Mantle layering from ScS reverberations: 2. The transition zone. *Journal of Geophysical Research: Solid Earth, 96*(B12), 19763-19780.

Ritsema, J., Deuss, A. A., Van Heijst, H. J., & Woodhouse, J. H., 2011. S40RTS: a degree-40 shear-velocity model for the mantle from new Rayleigh wave dispersion, teleseismic traveltime and normal-mode splitting function measurements. *Geophysical Journal International*, *184*(3), 1223-1236.

Ritsema, J., Van Heijst, H.J. and Woodhouse, J.H., 2004. Global transition zone tomography. *Journal of Geophysical Research: Solid Earth, 109*(B2).

671 Rychert, C. A., Rondenay, S., & Fischer, K. M., 2007. P-to-S and S-to-P imaging of a sharp lithosphere-asthenosphere
672 boundary beneath eastern North America. *Journal of Geophysical Research: Solid Earth*, *112*(B8).

673 Shearer, P. M., 1990. Seismic imaging of upper-mantle structure with new evidence for a 520-km discontinuity.
674 *Nature*, *344*(6262), 121-126.

675 Shearer, P.M., 1991. Constraints on upper mantle discontinuities from observations of long-period reflected and
676 converted phases. *Journal of Geophysical Research: Solid Earth, 96*(B11), pp.18147-18182.

677 Shearer, P. M., & Buehler, J., 2019. Imaging upper-mantle structure under USArray using long-period reflection
678 seismology. *Journal of Geophysical Research: Solid Earth*, *124*(9), 9638-9652.

679 Tromp, J., Tape, C., & Liu, Q., 2005. Seismic tomography, adjoint methods, time reversal and banana-doughnut
680 kernels. *Geophysical Journal International, 160*(1), 195-216.

681 Van der Lee, S., & Nolet, G., 1997. Upper mantle S velocity structure of North America. *Journal of Geophysical*
682 *Research: Solid Earth*, *102*(B10), 22815-22838.

683 Xu, W., Lithgow-Bertelloni, C., Stixrude, L. and Ritsema, J., 2008. The effect of bulk composition and temperature
684 on mantle seismic structure. *Earth and Planetary Science Letters, 275*(1-2), pp.70-79.

685 Zhao, L., & Chevrot, S., 2003. SS-wave sensitivity to upper mantle structure: Implications for the mapping of
686 transition zone discontinuity topographies. *Geophysical research letters, 30*(11).